Title

Expansion Revealing: Decrowding Proteins to Unmask Invisible Brain Nanostructures

Authors

Deblina Sarkar[1,2,14], Jinyoung Kang[3,14], Asmamaw T Wassie[4,14], Margaret E. Schroeder[3,5], Zhuyu Peng[5,6], Tyler B. Tarr[7], Ai-Hui Tang[7,8], Emily Niederst[6], Jennie Z. Young[5,6], Li-Huei Tsai[5,6,9*], Thomas A. Blanpied[7,10*], Edward S. Boyden[2,3,4,5,11, 12,13*]

Affiliations

[1]Media Lab, MIT, Cambridge, MA, USA.

[2]MIT Center for Neurobiological Engineering, MIT, Cambridge, MA, USA.

[3]MIT McGovern Institute for Brain Research, MIT, Cambridge, MA, USA.

[4]Department of Biological Engineering, MIT, Cambridge, MA, USA.

[5]Department of Brain and Cognitive Sciences, MIT, Cambridge, MA, USA.

[6]The Picower Institute for Learning and Memory, MIT, Cambridge, MA, USA.

[7]Department of Physiology, University of Maryland School of Medicine, Baltimore, MD, USA

[8]Key Laboratory of Brain Function and Disease and Hefei National Laboratory for Physical Sciences at the Microscale, Division of Life Sciences and Medicine, University of Science and Technology of China, Hefei, China

[9]Broad Institute of MIT and Harvard, Cambridge, MA, USA

[10]Program in Neuroscience, University of Maryland School of Medicine, Baltimore, MD, USA

[11]Koch Institute, MIT, Cambridge, MA, USA

[12]Howard Hughes Medical Institute, Cambridge, MA, USA

[13]Media Arts and Sciences, MIT, Cambridge, MA, USA

[14]These authors contributed equally.

*e-mail: edboyden@mit.edu, lhtsai@mit.edu, TBlanpied@som.umaryland.edu

Abstract

Expansion microscopy[1,2] is an increasingly widespread technology for nanoimaging, because its precise physical magnification of biological specimens enables ordinary microscopes to achieve nanoscale effective resolutions. Fluorescent labels such as antibodies can be applied either before or after expansion, with the latter offering the potential for better access to proteins within densely packed environments[3–7]. We here assess this possibility of epitope decrowding through physical expansion of proteins away from each other, using a 20x expansion protocol that we call expansion revealing (ExR), by labeling, within intact brain circuits, the same set of synaptic proteins both pre- and post-expansion. This comparison shows that post-expansion labeling introduces minimal spatial error and off-target staining relative to pre-expansion staining, while revealing the presence of proteins that are invisible when stained pre-expansion. Using ExR, we show in intact brain tissue the alignment of presynaptic calcium channels with postsynaptic machinery in nanocolumns, which may facilitate precision synaptic transmission, as well as the existence of periodic amyloid-containing nanoclusters containing ion channel proteins in Alzheimer's model mice, which may help generate novel hypotheses for Alzheimer's pathology and neural excitability. Thus, the decrowding power of ExR is able to reveal novel nanostructures within intact brain circuitry, and may find broad use in biology and medicine for unmasking nanostructures of importance in normal functions and disease.

Main Text

Introduction

Because proteins are nanoscale and often organized with nanoscale precision in cells and tissues, there is great demand for simple, powerful methods of nanoimaging of proteins in the context of intact biological specimens. In expansion microscopy (ExM) visualization of proteins in cells and tissues, proteins or fluorescent antibodies targeted to proteins are covalently anchored to a swellable hydrogel that is densely (mesh size of a few nanometers) and evenly synthesized throughout a preserved biological specimen[1]. Then the specimen is softened through treatment via enzymatic, detergent, and/or heat treatment, followed by physical expansion by adding water, and then optionally labeled with fluorescent stains, before imaging on a microscope. Because ExM protocols physically expand biological specimens, typically by factors of 4x-20x in linear dimension, and the process is isotropic and homogeneous down to nanoscale dimensions, they enable nanoimaging on conventional, diffraction limited microscopes, and are finding use throughout biology and medicine[2]. Although most ExM studies add antibodies to bind to and label proteins before expansion, because that allows antibodies to be administered to a sample in a familiar and conventional (i.e., unexpanded) state[8], there is increasing interest in expanding proteins away from each other and then adding antibodies post-expansion, because that would reduce the spatial error introduced by the nonzero size of the antibody itself, and also because of the possibility of decrowding proteins away from each other for better antibody access[3–7]. Could such a decrowding strategy reveal fundamentally new nanostructures within complex biological specimens? That is a tricky question to answer because of potential concerns that the decrowding process may introduce artifacts – for example, facilitating nonspecific binding of antibodies, or introducing fine-scale distortion relative to pre-expansion staining. Thus, we here systematically

probe this question, by labeling synaptic proteins within an individual brain specimen both pre-expansion and post-expansion, so that within densely packed structures such as synapses, we can precisely gauge exactly what signal is added during the process of post-expansion staining, and so that we can also gauge any distortion that is added by the process of post-expansion staining. We find that the amount of spatial error introduced by post-expansion staining is small, perhaps 10 nm, that the staining is precise and detailed, and that indeed post-expansion staining can reveal epitopes that are invisible pre-expansion; together, these capabilities are capable of revealing new nanostructures in intact brain tissue, including important components of synaptic nanocolumns, as well as periodic nanostructures that may be of relevance to Alzheimer's disease.

Expansion revealing: a method for expanding brain tissues 20x while retaining proteins

To enable this analysis, we developed a powerful yet simple protocol for 20x expansion of cells and tissues (**Fig. 1a-c**), which iteratively expands a specimen twice, in a fashion that retains proteins throughout both expansion steps, and that uses all off-the-shelf chemicals. We reasoned that one could expand a brain specimen through one round of gelation and expansion, and that this first swellable hydrogel could then be further expanded if we formed a second swellable hydrogel in the space opened up by the first expansion, and then swelled the specimen a second time (see Methods for details). The proteins, being anchored to the first hydrogel, would be retained because the original hydrogel would be further expanded by the second swellable hydrogel, and not cleaved or discarded. This strategy avoids the need to transfer biomolecular information from the first hydrogel to the second one, which is challenging and, in our earlier form of iterative expansion microscopy (iExM), was mediated by a DNA intermediate that necessitated loss of the original biomolecules[9]. Then, proteins can be antibody labeled in the final step (**Fig. 1c**), after decrowding

and before imaging, enabling visualization of proteins that would have been missed if stained in the crowded state (**Fig. 1b**). We call this protocol expansion revealing (ExR).

We first quantified the global isotropy of the expansion process, and found a similar low distortion (i.e., of a few percent over length scales of tens of microns, **Supp. Fig. 1**) as we did for previous ExM protocols[1,3,9–11]. As with previous protocols, to measure effective resolution, we focused on synapses, given both their importance for neural communication and utility as a super-resolution testbed, staining post-expansion cortical synapses (**Fig. 1d**) with antibodies against the pre-synaptic protein Bassoon and the post-synaptic proteins PSD95 and Homer1 (**Fig. 1e-1g**). We found that when we measured the mean distance between domains containing the proteins PSD95, Homer1, and Shank3, we obtained values (**Fig. 1h**) that were very similar to classical results found using STORM microscopy[12] (note that our study focused on Shank3 and this earlier study focused on Shank1). Thus, ExR exhibits comparable effective resolution, on the order of ~20 nm, to our earlier iExM protocol, which did not retain proteins[9].

High-fidelity enhancement of synaptic protein visualization via ExR

To gauge whether ExR could reveal nanostructures in the brain that were not visible through pre-expansion staining, and to further probe whether the post-expansion staining incurred any costs in terms of decreased resolution or added distortion relative to classical pre-expansion staining, we devised a strategy where we would stain brain slices pre-expansion with an antibody against a synaptic protein, in a fashion so that antibodies would be anchored to the expansion hydrogel for later visualization, then perform ExR, and then restain the same proteins with the same antibody a

second time, thus enabling a within-sample comparison of a given protein across both conditions, which could reveal any nanostructural differences. For pre-expansion staining (see Methods for details), we immunostained mouse brain slices containing somatosensory cortex (**Fig. 2a**) with primary antibodies followed by 6-((acryloyl)amino)hexanoic acid, succinimidyl ester (abbreviated AcX)-conjugated secondary antibodies, so that these antibodies could be attached to the swellable hydrogel for post-expansion tertiary antibody staining and visualization. This allowed us to compare pre-ExR staining to post-ExR staining, at the same resolution level, and for the same field of view, important for noticing any changes in nanostructural detail. We noted that Homer1 and Shank3 exhibited very similar visual appearances when we compared pre- vs. post-ExR staining (quantified below), so we designated these two stains as "reference channels," that is, co-stains that could help define synapses for the purposes of technological comparison, and that we could use to help us gauge whether other proteins were becoming more visible at synapses.

We chose 7 synaptic proteins important for neural architecture and transmission for this experiment – the presynaptic proteins Bassoon, RIM1/2, and the P/Q-type Calcium channel $Ca_v2.1$ alpha 1A subunit, and the postsynaptic proteins Homer1, Shank3, SynGAP, and PSD95 (**Fig. 2b-h**), staining for each protein along with a reference channel stain (note, when we imaged Homer1, we used Shank3 as the reference channel, and vice versa). All seven proteins exhibited well-defined images when post-expansion stained, with the geometry reflecting characteristic synaptic shapes. For example, using a presynaptic and a postsynaptic stain (**Fig. 2b, 2c, 2g**) revealed parallel regions with a putative synaptic cleft in between (although note that this was only visible if the synapse was being imaged from the side; if a synapse was being imaged with the axial direction of the microscope perpendicular to the synaptic cleft, then the image may look more disc-

shaped)[9,12,13]. In many cases, however, post-ExR staining revealed more detailed structures of synapses compared to what was visualized with pre-expansion staining – for example, calcium channels (**Fig. 2b)**, RIM1/2 **(Fig. 2c**), PSD95 (**Fig. 2d**), SynGAP (**Fig. 2e**), and Bassoon (**Fig. 2g**) appeared more prominent post-expansion than pre-expansion. Applying a conventional antigen retrieval protocol did not result in such improvements (**Supp. Fig. 2**), suggesting that the decrowding effect observed via ExR was indeed due to expansion, and not simply due to denaturation or antigen retrieval-like effects associated with other aspects of the ExR process.

To quantitate the improvement in staining enabled by ExR, we measured the amplitude and volume of each synaptic protein stain, both within, and just outside of, identified synapses. First, we manually identified between 49-70 synapses (see **Supplementary Table 1** for exact numbers) per ~350x350x20 μm^3 (in physical units, e.g. what is actually seen through the microscope lens) field of view, choosing the largest and brightest synapses based on reference channel staining (i.e., Homer1 or Shank3). We developed an automated method to segment synaptic puncta from nearby background. Briefly, we created binary image stacks for each channel using a threshold equal to a multiple of the average measured standard deviation of five manually-identified background regions (not blinded to condition), filtered 3D connected components based on size, and used dilated reference channel ROIs to segment putative synaptic puncta (**Supplementary Fig. 3** and Methods). We dilated reference channel-defined ROIs to relax the requirement of exact colocalization of pre-synaptic proteins with a post-synaptic reference. We found that post-expansion staining increased signal intensity and mean total volume of signal within dilated reference-channel defined ROIs, without meaningfully affecting background (i.e., signal just outside the dilated reference channel-defined ROIs) staining (**Fig. 2i-j**). In summary, all proteins

except Homer1 and PSD95 showed significantly increased signal intensity of post-expansion staining within dilated reference ROIs, with minimal increase in the background (**Fig. 2i;** see **Supplementary Table 2** for full statistical analysis). (We note that there was no change in signal intensity in the background for PSD95, but a bimodal distribution of signal intensity increase in the foreground, potentially due to poor signal quality in one animal.) Similarly, all proteins exhibited increased total volume of post-expansion staining signals within dilated references ROIs, and minimal or no increase in the volume of background ROIs (**Fig. 2j**; see **Supplementary Table 3** for full statistical analysis). Because Homer1 and Shank3 had the smallest changes in pre- vs. post-expansion staining, they were chosen as reference channels to indicate the locations of putative synapses for pre- vs. post-expansion test stain comparison, as mentioned above. Of course, different antibodies may bind to different sites on a target protein, and we found that a different antibody against PSD95 (from Cell Signaling Technology, product number CST3450S) than the one used in **Fig. 2** (Thermofisher, product number MA1-046) showed similar signal intensity and volume when compared pre- vs. post-staining (**Supplementary Fig. 4)**; perhaps, in future studies, the use of multiple antibodies against different parts of a single protein, in pre- vs. post-expansion comparisons, could be used to gauge the density of the environment around different parts of that protein.

We further analyzed synaptic protein signals pre- vs. post-expansion in the context of different cortical layers. We quantified volume and signal-to-noise ratio (SNR; signal intensity divided by standard deviation of the background) of each protein in 3D synaptic structures by binarizing signals over a threshold (a multiple of the standard deviation of the intensity within a manually-selected background region; see Methods) and selecting putative synapses in each ~350x350x20

μm^3 field of view imaged above, comparing the values of pre- vs. post-expansion staining in each layer of somatosensory cortex (L1, L2/3 and L4, respectively) (**Fig. 2k-l**). Post-expansion volumes exhibited larger volumes in each layer for all of the stains except for the reference channel stains, and improved SNR for all synaptic proteins (see **Supplementary Tables 4** and **5** for full statistics).

In previous work, we showed using the iterative expansion microscopy (iExM) protocol, which uses pre-expansion staining, that we could achieve effective resolutions of ~20 nm, with low distortion due to the expansion process[9]. As another independent way to gauge the potential distortion obtained by staining with antibodies post-expansion, we compared the shapes of synaptic puncta as seen with the pre-expansion stain, with the shapes as seen with the new post-expansion stain, using the within-sample dual staining method used in **Fig. 2a-l.** We compared various properties of synaptic puncta between pre- and post-expansion staining conditions, using the reference proteins Homer1 and Shank3 since they had similar intensities and volumes when comparing pre- and post-expansion datasets, and therefore might be appropriate for comparing shape features across these conditions (**Supplementary Fig. 5)**. In summary, we did not see significant distortion being introduced by post-expansion staining; for example, we found no significant difference in the number of synaptic puncta when we compared pre- vs. post-expansion staining in the same sample (**Fig. 2m**), and when we measured the shift in puncta positions between pre- and post-stained conditions, we observed average shifts of <10nm (in biological units, i.e. physical size divided by the expansion factor) between post- and pre-expansion staining for both Homer1 and Shank3 (**Fig. 2n-o**; please see **Supplementary Table 4** for full statistics). Thus ExR preserves, relative to classical pre-expansion staining, the locations of proteins with high fidelity for the purposes of post-expansion staining.

Synaptic nanocolumns coordinated with calcium channel distributions

Coordinating pre- and post-synaptic protein arrangement in a nanocolumn structure which aligns molecules within the two neurons contributes to precision signaling from presynaptic release sites to postsynaptic receptor locations[13,14], as well as to the long-term plasticity of synaptic function[15]. Given that ExR is capable of unmasking synaptic proteins that are otherwise not detectable, with nanoscale precision, we next sought to explore the nanocolumnar architecture of pre- and postsynaptic proteins, with a focus on important molecules that have not yet been explored in this transsynaptic alignment context. As noted above, ExR greatly helps with visualization of calcium channels, which of course are amongst the most important molecules governing the activation of synaptic release machinery, with nanometer-scale signaling contributing to the precision of synaptic vesicle fusion. However, the nanoscale mapping of calcium channels in the context of nanocolumnar alignment in intact brain circuits remains difficult[16–18] (**Fig. 2b**). We thus applied ExR to investigate whether calcium channels occupy nanocolumns with other pre- and post-synaptic proteins, such as the critical pre- and post-synaptic proteins RIM1/2 and PSD95, respectively, across the layers of the cortex (**Fig. 3a-d**). We first performed a 3D autocorrelation function ($g_a(r)$)-based test which provides information about the intensity distribution within a defined structure (see Methods). Any heterogeneity in the intensity distribution within the cluster will result in a $g_a(r)>1$, and the distance at which the $g_a(r)$ crosses 1 can be used to estimate the size of the internal heterogeneity, here termed a nanodomain[13]. In all cortical layers, our auto-correlation analysis shows that all 3 proteins explored exhibited a non-uniform arrangement forming nanodomains with average diameters of about 60-70nm (in biological units; **Fig. 3e-h**). To analyze the spatial relationship between the two distributions and the average molecular density

of RIM1/2, PSD95 and $Ca_v2.1$ relative to each other, we performed a protein enrichment analysis, which is a measure of volume-averaged intensity of one channel as a function of distance from the peak intensity of another channel (see Methods). To more easily compare the extent of the enrichment between these proteins in each layer, we also calculated the enrichment index, which is an average of all enrichment values within 60 nm (biological units) of the peak of a designated channel. Our analysis shows that the centers of nanodomains of RIM1/2, PSD95 and $Ca_v2.1$ are enriched with respect to each other (**Fig. 3i-p**). Of particular interest, the nanoscale colocalization of $Ca_v2.1$ with RIM1/2 (and thus the vesicle site) likely minimizes the distance between the channels and the molecular Ca sensors that trigger vesicle fusion (**Fig. 3q-r**), consistent with the physiological concept of nanodomain coupling that tunes the efficacy and frequency-dependence of neurotransmission[19]. Furthermore, the precise alignment between RIM1/2 and PSD95 may reduce the distance that released neurotransmitter needs to diffuse before reaching postsynaptic receptors (**Fig. 3r**). Thus, these nanoscale arrangements may help to optimize the speed, strength, and plasticity of synaptic transmission. To the best of our knowledge, this is the first report of the 3D nano-architecture of voltage gated calcium channel distributions within the transsynaptic framework probed in intact brain circuitry.

Periodic amyloid nanostructures in Alzheimer's model mouse brain

In addition to densely crowded proteins in healthy functioning compartments like synapses, densely crowded proteins appear in pathological states like Alzheimer's disease. Protein aggregates known as β-amyloid are thought to play roles in synaptic dysfunction, neurodegeneration and neuroinflammation[20]. However, the densely packed nature of these aggregates may make the nanoscale analysis of their ultrastructure within intact brain contexts

difficult to understand. To understand the nanoarchitecture of β-amyloid in the cellular context of intact brain circuitry, we applied ExR to the brains of 5xFAD Alzheimer's model mice **(Fig. 4a)**, as this widely used animal model of Alzheimer's exhibits an aggressive amyloid pathology[21]. We employed two different commercially available antibodies for β-amyloid, 6E10 (which binds to amino acid residues 1-16 of human Aβ peptides) and 12F4 (which is reactive to the C-terminus of human Aβ and has specificity towards Aβ42). We were particularly interested in investigating the relationship of amyloid deposits and white matter tracts, as these regions have been implicated in human imaging data[22–25], but are less investigated in mouse models. We previously reported the accumulation of Aβ aggregates along the fornix, the major white matter tract connecting the subiculum and mammillary body, early in disease progression[25]. We co-stained the amyloid antibodies along with the axonal marker SMI-312, and compared pre-expansion staining with that obtained after ExR. Plaques appeared to be larger, and to have finer-scaled features in post-expansion staining, than in pre-expansion staining (**Fig. 4b-4c**), when visualized by either 6E10 or 12F4 antibodies, and thus the post-expansion staining may unveil aspects of plaque geometry that are not easily visualized through traditional means. Additionally, post-ExR staining revealed detailed nanoclusters of β-amyloid that were not seen when staining was done pre-expansion **(Fig. 4b-c)**. These nanodomains of β-amyloid appeared to occur in periodic structures **(Fig. 4b-c, subpanels (i)-(iv))**. Co-staining with 2 different β-amyloid antibodies, D54D2 (which binds to isoforms Aβ37, Aβ38, Aβ40, and Aβ42) along with 6E10 or 12F4 in ExR-processed 5xFAD fornix showed similar patterns of periodic nanostructures, which means the observed periodic nanostructures are likely not composed of specific isoforms (**Supplementary Fig. 6**). These nanodomains, and periodic structures thereof, were not visualized through pre-expansion staining, which was confirmed using unexpanded tissue as well **(Supplementary Fig. 7)**. To see whether

the periodic nanostructures of β-amyloid revealed through ExR were just nonspecific staining artifacts of ExR, we performed ExR on wild type (WT) mice as a control, which should not have any labeling for human β-amyloid. As is clear from **Fig. 4d**, no β-amyloid structures were observed in ExR-processed WT brain slice. Our quantitative analysis examining the volume of amyloid in ExR-processed WT and 5xFAD mice confirms that there is indeed a large amount of amyloid volume occupied in 5xFAD samples, but essentially no such volume occupied in ExR-processed WT mice **(Fig. 4e)**. The lack of amyloid staining in ExR-processed WT mice makes it unlikely that the staining seen in ExR-processed 5xFAD mouse brain is nonspecific, and thus it is likely that the effect of ExR was to decrowd dense amyloid nanostructures that ordinarily hamper antibody staining.

Coclustering of amyloid nanodomains and ion channels

To understand the biological context of these periodic Aβ nanostructures, we stained brain slices with antibodies against the ion channels $Na_v1.6$ and $K_v7.2$. In myelinated axons, K_v7 potassium channels and voltage gated sodium (Na_v) channels colocalize tightly with nodes of Ranvier periodically along axons, while $Na_v1.6$ and $K_v7.2$ are diffusely distributed along unmyelinated axons[26]. Additionally, Alzheimer's is associated with altered neuronal excitability and alterations in ion channels[27]. We stained ExR-processed 5xFAD fornix-containing brain slices with antibodies against potassium channels ($K_v7.2$) and against β-amyloid (12F4) (**Fig. 5a, Supplementary Fig. 8**). The periodic β-amyloid nanostructures colocalized with periodic nanoclusters of potassium channels. In ExR-processed WT fornix, such β-amyloid clusters, and clusters of potassium channel staining, were not found (**Supplementary Fig. 9**). Co-staining of β-amyloid (12F4) and sodium channels ($Na_v1.6$) showed complementary results (**Supplementary Fig. 10**). To probe these

periodicities and relationships further, we obtained a cross-sectional profile of a stretch of axon, showing that Aβ42 (magenta) and Kv7.2 (yellow) were highly overlapping and with similar periodicities (**Fig. 5b**). A further histogram analysis showed the periodicity of both repeated protein structures to be 500-1000 nm (**Fig. 5c**), which we confirmed by Fourier analysis (**Fig. 5d-e**). This periodicity is notably higher in spatial frequency than the inter-node-of-Ranvier distances of brain white matter, which range from 20-100μm[28–30]. Our analysis along individual segments of axons also showed that a high fraction of Aβ42 clusters contained K_v7.2 clusters **(Fig. 5f)**, a result that we confirmed by measuring the distance between the centroids of overlapping Aβ42 and K_v7.2 nanoclusters, finding extremely tight colocalization, within a few tens of nanometers (**Fig. 5g**). Median sizes of nanoclusters were around 150nm for both Aβ42 and K_v7.2 (**Fig. 5h**); indeed, overlapping nanodomains of Aβ42 and K_v7.2 were highly correlated in size (**Fig. 5j**), suggesting a potential linkage between how they are formed and organized as multiprotein complexes.

To facilitate visualization of the 3D shapes of these Aβ42 and K_v7.2 puncta, we show three orthogonal slices in the x-y, x-z, and y-z planes (x- and y-directions being transverse directions, and the z-direction being axial) that intersect the center of each puncta. Qualitatively, we observed that the majority of these puncta are oblong, with smooth, continuous Aβ42 ellipsoids and more punctate K_v7.2 puncta, with some, but not all, K_v7.2 puncta found within Aβ42 puncta. A larger volume of Aβ42 (as a fraction of total Aβ42 puncta volume) was found inside Kv7.2 puncta compared to the fraction of Kv7.2 volume inside Aβ42 puncta (**Fig. 5k**). On average, the mean volume of an Aβ42 puncta was slightly larger than that of a Kv7.2 puncta (**Supplementary Fig. 11b,** paired t-test, $p = 0.0001$, $t=4.116$, $df=54$). Quantification of shape

characteristics confirmed these observations and revealed more subtle patterns. Representative images illustrating the observed trends are shown below each plot (**Fig. 5kii-nii**). Despite the larger volume of Aβ42 puncta, the fraction of Aβ42 volume mutually overlapped with (inside of) K_v7.2 puncta was larger than the fraction of K_v7.2 mutually overlapped with (inside of) Aβ42 puncta (**Fig. 5k**; $p < 0.0001$, t=10.94, df=54). When considering the ellipsoidal shapes of these puncta, the relationship between the second and first principal axis lengths was highly sublinear (**Fig. 5l**), and the average aspect ratio (ratio of first to second principal axis length) was ~3.5:1 (mean 3.464, standard deviation 1.911, n = 55 puncta), indicating a highly oblong shape (slope of best-fit line from simple linear regression = 0.05883, p = 0.0020, F = 10.59, df = 53). While the number of K_v7.2 present in each manually cropped ROI was not correlated with the volume of the largest Aβ42 puncta within the cropped ROI (**Supplementary Fig. 11c**; simple linear regression, 95% CI for slope [-0.003940, 0.005947]), the mean Kv7.2 puncta volume was significantly correlated with the mean Aβ42 puncta volume (**Supplementary Fig. 11d**; simple linear regression, 95% CI of slope [0.09878-0.2437], $R^2 = 0.2977$, $p < 0.0001$, F = 22.47, df = 53). Thus, as the size of Aβ42 aggregates increases, K_v7.2 aggregates increase in size, but not number. We found that the volume of K_v7.2 puncta inside Aβ42 puncta is highly correlated with the volume of the Aβ42 puncta (**Fig. 5m**; simple linear regression, 95% CI of slope [0.8353-9037], $R^2 = 0.98$, $p < 0.0001$, F = 2,593, df = 53), but the volume of K_v7.2 puncta outside of Aβ42 puncta is not correlated to Aβ42 puncta volume (**Fig. 5m**; simple linear regression, 95% CI of slope [-0.03919, 0.4503], $R^2 = 0.05082$, p = 0.0929, F = 2.838, df = 53). Conversely, the total volume of Aβ42 puncta inside of K_v7.2 puncta was not as strongly correlated (**Fig. 5n**; simple linear regression, 95% CI of slope [0.4198, 0.6307], $R^2 = 0.6531$, $p < 0.0001$, F = 99.29, df = 53) with the volume of the largest K_v7.2 puncta in the cropped ROI. The volume of Aβ42 puncta

outside of $K_v7.2$ was weakly but significantly correlated to the size of the largest $K_v7.2$ puncta (**Fig. 5n**; 95% CI of slope [0.0250, 0.09245] $R^2 = 0.1876$, $p = 0.0010$, $F = 12.24$, df = 53). Finally, we found that the non-overlapped volume as a function of overlapped volume was much larger, on average, for $K_v7.2$ than for Aβ42 (**Supplementary Fig. 11e**; paired t-test, $p < 0.0001$, t=5.985, df=54). Taken together, these results show that $K_v7.2$ and Aβ42 puncta are correlated in size only when physically colocalized in a tightly registered fashion, perhaps pointing to new potential hypothesized mechanisms of aggregation. While the biological relevance of this periodicity and colocalization of β-amyloid with $K_v7.2$ and $Na_v1.6$ needs further investigation, it is interesting to note that, $Na_v1.6$ and $K_v7.2$ ion channels can regulate neural excitability[31–33], and Aβ peptides have also been known to influence excitability[34]. As these Aβ structures were often, but not always, colocalized with SMI-positive axons, and are highly reactive for Aβ42, we interpret these structures as periodic amyloid depositions. In the future, it will be interesting to see whether these structures play direct roles in neural hyperexcitability in Alzheimer's.

It is curious to reflect here that periodicity and order[35–45] are often thought of as associated with healthy biological systems, whose functionality is supported by such crystallinity. On the other hand, disorder, misalignments and misfoldings are often tied to pathological states. Here we find a curious mixture of the two – a periodicity that seems to be associated with a pathological state, and that may have implications for new hypotheses related to Alzheimer's pathology. We are excited to see how ExR might reveal many new kinds of previously invisible nanopatterns in healthy and disease states, due to its ease of use and applicability to multiple contexts, as here seen.

Main References

1. Chen, F., Tillberg, P. W. & Boyden, E. S. Expansion microscopy. *Science* **347**, 543–548 (2015).
2. Wassie, A. T., Zhao, Y. & Boyden, E. S. Expansion microscopy: principles and uses in biological research. *Nature Methods* vol. 16 33–41 (2019).
3. Tillberg, P. W. *et al.* Protein-retention expansion microscopy of cells and tissues labeled using standard fluorescent proteins and antibodies. *Nat. Biotechnol.* **34**, 987–992 (2016).
4. Ku, T. *et al.* Multiplexed and scalable super-resolution imaging of three-dimensional protein localization in size-adjustable tissues. *Nat. Biotechnol.* **34**, 973–981 (2016).
5. M'Saad, O. & Bewersdorf, J. Light microscopy of proteins in their ultrastructural context. *Nat. Commun.* 1–15 (2020) doi:10.1101/2020.03.13.989756.
6. Gambarotto, D. *et al.* Imaging cellular ultrastructures using expansion microscopy (U-ExM). *Nat. Methods* **16**, 71–74 (2019).
7. Zwettler, F. U. *et al.* Molecular resolution imaging by post-labeling expansion single-molecule localization microscopy (Ex-SMLM). *Nat. Commun.* **11**, 1–11 (2020).
8. Asano, S. M. *et al.* Expansion Microscopy: Protocols for Imaging Proteins and RNA in Cells and Tissues. *Curr. Protoc. Cell Biol.* **80**, (2018).
9. Chang, J. B. *et al.* Iterative expansion microscopy. *Nat. Methods* **14**, 593–599 (2017).
10. Chen, F. *et al.* Nanoscale imaging of RNA with expansion microscopy. *Nat. Methods* **13**, 679–684 (2016).
11. Zhao, Y. *et al.* Nanoscale imaging of clinical specimens using pathology-optimized expansion microscopy. *Nat. Publ. Gr.* **35**, (2017).
12. Dani, A., Huang, B., Bergan, J., Dulac, C. & Zhuang, X. Superresolution Imaging of

Chemical Synapses in the Brain. *Neuron* **68**, 843–856 (2010).

13. Tang, A. H. *et al.* A trans-synaptic nanocolumn aligns neurotransmitter release to receptors. *Nature* **536**, 210–214 (2016).

14. Heine, M. & Holcman, D. Asymmetry Between Pre- and Postsynaptic Transient Nanodomains Shapes Neuronal Communication. *Trends in Neurosciences* vol. 43 182–196 (2020).

15. Hruska, M., Henderson, N., Marchand, S. J. Le, Jafri, H. & Dalva, M. B. Synaptic nanomodules underlie the organization and plasticity of spine synapses. *Nat. Neurosci.* **21**, 671–682 (2018).

16. Rebola, N. *et al.* Distinct Nanoscale Calcium Channel and Synaptic Vesicle Topographies Contribute to the Diversity of Synaptic Function. *Neuron* **104**, 693-710.e9 (2019).

17. Brockmann, M. M. *et al.* RIM-BP2 primes synaptic vesicles via recruitment of Munc13-1 at hippocampal mossy fiber synapses. *Elife* **8**, (2019).

18. Holderith, N. *et al.* Release probability of hippocampal glutamatergic terminals scales with the size of the active zone. *Nat. Neurosci.* **15**, 988–997 (2012).

19. Eggermann, E., Bucurenciu, I., Goswami, S. P. & Jonas, P. Nanodomain coupling between Ca 2+ channels and sensors of exocytosis at fast mammalian synapses. *Nature Reviews Neuroscience* vol. 13 7–21 (2012).

20. Canter, R. G., Penney, J. & Tsai, L. H. The road to restoring neural circuits for the treatment of Alzheimer's disease. *Nature* vol. 539 187–196 (2016).

21. Oakley, H. *et al.* Intraneuronal β-amyloid aggregates, neurodegeneration, and neuron loss in transgenic mice with five familial Alzheimer's disease mutations: Potential factors in amyloid plaque formation. *J. Neurosci.* **26**, 10129–10140 (2006).

22. Chao, L. L. *et al.* Associations between White Matter Hyperintensities and β Amyloid on Integrity of Projection, Association, and Limbic Fiber Tracts Measured with Diffusion Tensor MRI. *PLoS One* **8**, e65175 (2013).

23. Song, S. K., Kim, J. H., Lin, S. J., Brendza, R. P. & Holtzman, D. M. Diffusion tensor imaging detects age-dependent white matter changes in a transgenic mouse model with amyloid deposition. *Neurobiol. Dis.* **15**, 640–647 (2004).

24. Dong, J. W. *et al.* Diffusion MRI biomarkers of white matter microstructure vary nonmonotonically with increasing cerebral amyloid deposition. *Neurobiol. Aging* **89**, 118–128 (2020).

25. Gail Canter, R. *et al.* 3D mapping reveals network-specific amyloid progression and subcortical susceptibility in mice. *Commun. Biol.* **2**, 1–12 (2019).

26. Lubetzki, C., Sol-Foulon, N. & Desmazières, A. Nodes of Ranvier during development and repair in the CNS. *Nat. Rev. Neurol.* **16**, (2020).

27. Dunn, A. R. & Kaczorowski, C. C. Regulation of intrinsic excitability: Roles for learning and memory, aging and Alzheimer's disease, and genetic diversity. *Neurobiol. Learn. Mem.* **164**, 107069 (2019).

28. Chong, S. Y. C. *et al.* Neurite outgrowth inhibitor Nogo-A establishes spatial segregation and extent of oligodendrocyte myelination. *Proc. Natl. Acad. Sci. U. S. A.* **109**, 1299–1304 (2012).

29. Brohawn, S. G. *et al.* The mechanosensitive ion channel traak is localized to the mammalian node of ranvier. *Elife* **8**, 1–22 (2019).

30. Dupree, J. L. *et al.* Olirdendrocytes assist in the maintenance of sodium channel clusters independent of the myelin sheath. *Neuron Glia Biol.* **1**, 179–192 (2004).

31. Shah, N. H. & Aizenman, E. Voltage-Gated Potassium Channels at the Crossroads of Neuronal Function, Ischemic Tolerance, and Neurodegeneration. *Transl. Stroke Res.* **5**, 38–58 (2014).

32. Hessler, S. *et al.* β-secretase BACE1 regulates hippocampal and reconstituted M-currents in a β-subunit-like fashion. *J. Neurosci.* **35**, 3298–3311 (2015).

33. Ciccone, R. *et al.* Amyloid β-Induced Upregulation of Nav1.6 Underlies Neuronal Hyperactivity in Tg2576 Alzheimer's Disease Mouse Model. *Sci. Rep.* **9**, 1–18 (2019).

34. Ghatak, S. *et al.* Mechanisms of hyperexcitability in alzheimer's disease hiPSC-derived neurons and cerebral organoids vs. Isogenic control. *Elife* **8**, (2019).

35. Lim, C. J., Lee, S. Y., Teramoto, J., Ishihama, A. & Yan, J. The nucleoid-associated protein Dan organizes chromosomal DNA through rigid nucleoprotein filament formation in E. coli during anoxia. *Nucleic Acids Res.* **41**, 746–753 (2013).

36. Xu, K., Zhong, G. & Zhuang, X. Actin, spectrin, and associated proteins form a periodic cytoskeletal structure in axons. *Science* **339**, 452–456 (2013).

37. Bose, K., Lech, C. J., Heddi, B. & Phan, A. T. High-resolution AFM structure of DNA G-wires in aqueous solution. *Nat. Commun.* **9**, (2018).

38. Winardhi, R. S., Castang, S., Dove, S. L. & Yan, J. Single-molecule study on histone-like nucleoid-structuring protein (H-NS) paralogue in Pseudomonas aeruginosa: MvaU Bears DNA organization mode similarities to MvaT. *PLoS One* **9**, (2014).

39. Leterrier, C. *et al.* Nanoscale Architecture of the Axon Initial Segment Reveals an Organized and Robust Scaffold. *Cell Rep.* **13**, 2781–2793 (2015).

40. Chiang, Y. L. *et al.* Atomic force microscopy characterization of protein fibrils formed by the amyloidogenic region of the bacterial protein MinE on mica and a supported lipid

bilayer. *PLoS One* **10**, (2015).

41. Prakash, K. *et al.* Superresolution imaging reveals structurally distinct periodic patterns of chromatin along pachytene chromosomes. *Proc. Natl. Acad. Sci. U. S. A.* **112**, 14635–14640 (2015).

42. Makky, A., Bousset, L., Polesel-Maris, J. & Melki, R. Nanomechanical properties of distinct fibrillar polymorphs of the protein α-synuclein. *Sci. Rep.* **6**, (2016).

43. D'Este, E., Kamin, D., Göttfert, F., El-Hady, A. & Hell, S. W. STED Nanoscopy Reveals the Ubiquity of Subcortical Cytoskeleton Periodicity in Living Neurons. *Cell Rep.* **10**, 1246–1251 (2015).

44. D'Este, E. *et al.* Subcortical cytoskeleton periodicity throughout the nervous system. *Sci. Rep.* **6**, (2016).

45. Qu, Y., Hahn, I., Webb, S. E. D., Pearce, S. P. & Prokop, A. Periodic actin structures in neuronal axons are required to maintain microtubules. *Mol. Biol. Cell* **28**, 296–308 (2017).

Figures and Figure Legends

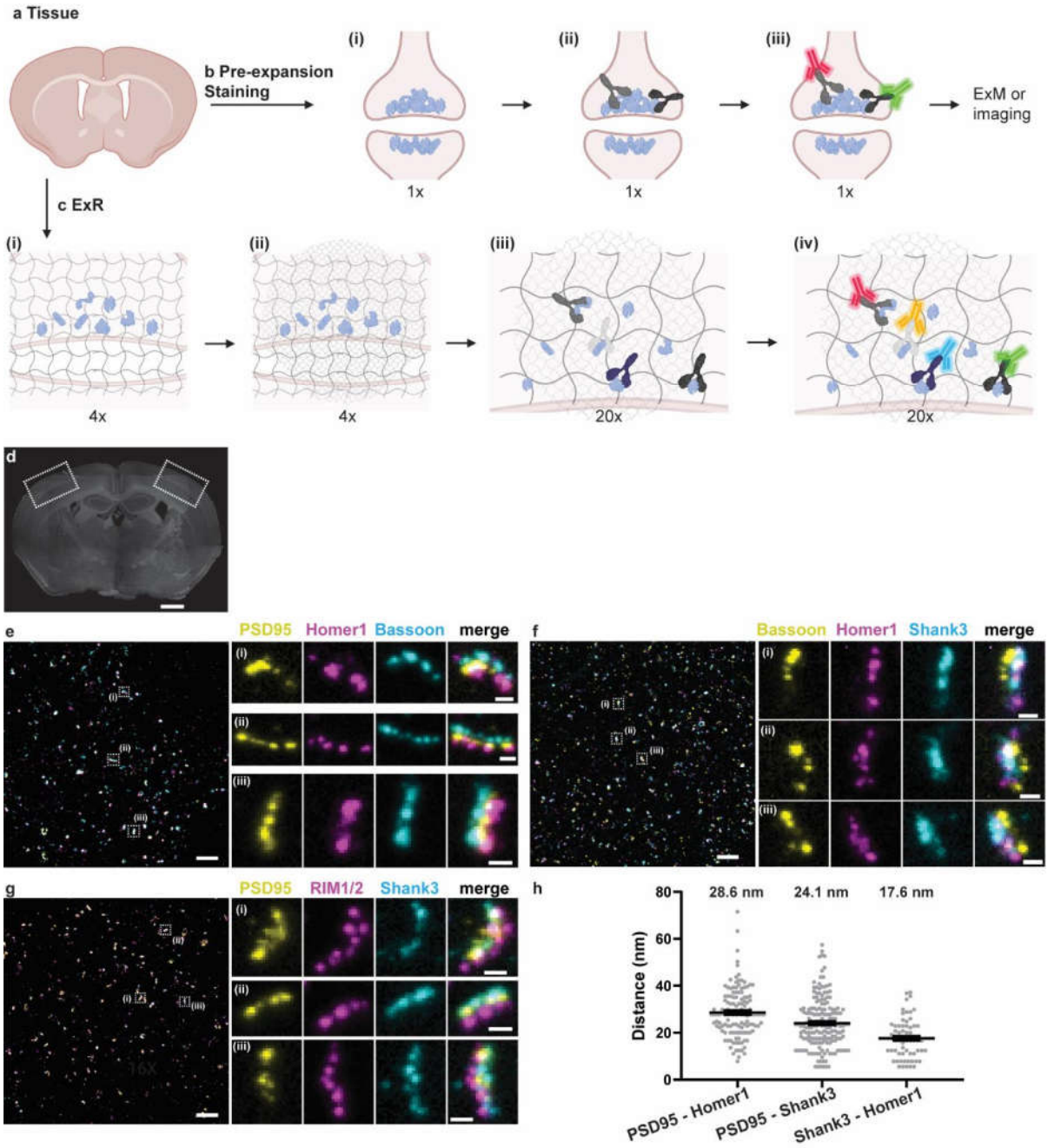

Figure 1 | Expansion Revealing (ExR), a technology for decrowding of proteins through isotropic protein separation. (a) Coronal section of mouse brain before staining or expansion.

(b) Conventional antibody staining may not detect crowded biomolecules, shown here in pre- and post-synaptic terminals of cortical neurons. **(bi)** Crowded biomolecules before antibody staining. (**bii)** Primary antibody (Y-shaped proteins) staining in non-expanded tissue. Antibodies cannot access interior biomolecules, or masked epitopes of exterior biomolecules. **(biii)** Secondary antibody (fluorescent green and red Y-shaped proteins) staining in non-expanded tissue. After staining, tissue can be imaged or expanded using earlier ExM protocols, but inaccessible biomolecules will not be detected. **(c)** Post-expansion antibody staining with ExR. **(ci)** Anchoring and first gelation step. Specimens are labeled with gel-anchoring reagents to retain endogenous proteins, with acrylamide included during fixation to serve as a polymer-incorporatable anchor, as in refs[4,6] . Subsequently, the specimen is embedded in a swellable hydrogel that permeates densely throughout the sample (gray wavy lines), mechanically homogenized via detergent treatment and heat treatment, and expanded in water. **(cii)** Re-embedding and second swellable gel formation gelation. The fully expanded first gel (expanded 4x in linear extent) is re-embedded in a charge-neutral gel (not shown), followed by the formation of a second swellable hydrogel (light gray wavy lines). **(ciii)** 20x expansion and primary antibody staining. The specimen is expanded by another factor of 4x, for a total expansion factor of ~20x, via the addition of water, then incubated with conventional primary antibodies. Because expansion has decrowded the biomolecules, conventional antibodies can now access interior biomolecules and additional epitopes of exterior molecules. **(civ)** Post-expansion staining with conventional fluorescent secondary antibodies (fluorescent blue and yellow Y-shaped proteins, in addition to the aforementioned red and green ones) to visualize decrowded biomolecules. Schematic created with BioRender.com. **(d)** Low-magnification widefield image of a mouse brain slice stained with DAPI, with box highlighting the somatosensory cortex used in subsequent figures for synapse staining (Scale bar, 500 μm), and (**e-g)** confocal images (max intensity projections) of representative fields of view (cortical L2/3) and specific synapses after ExR expansion and subsequent immunostaining using antibodies against (**e)** PSD95, Homer1, Bassoon; (**f)** Bassoon, Homer1, Shank3; and (**g**) PSD95, RIM1/2, Shank3. Scale bar, 1 μm , left image; 100 nm, right images; in biological units, i.e. the physical size divided by the expansion factor, throughout the paper unless otherwise indicated. **(h)** Measured distance between centroids of protein densities of PSD95 and Homer1, PSD95 and Shank3, and Shank3 and Homer1, in synapses such as those in panels **e-g**. The mean distance (again, in biological units) between PSD95 and Homer1 is 28.6 nm (n = 126 synapses from 3 slices from 1 mouse), between PSD95 and Shank3 is 24.1 nm (n=172 synapses from 3 slices from 1 mouse), and between Shank3 and Homer1 is 17.6 nm (n=70 synapses from 3 slices from 1 mouse). Plotted is mean +/- standard error; individual grey dots represent the measured distance for individual synapses.

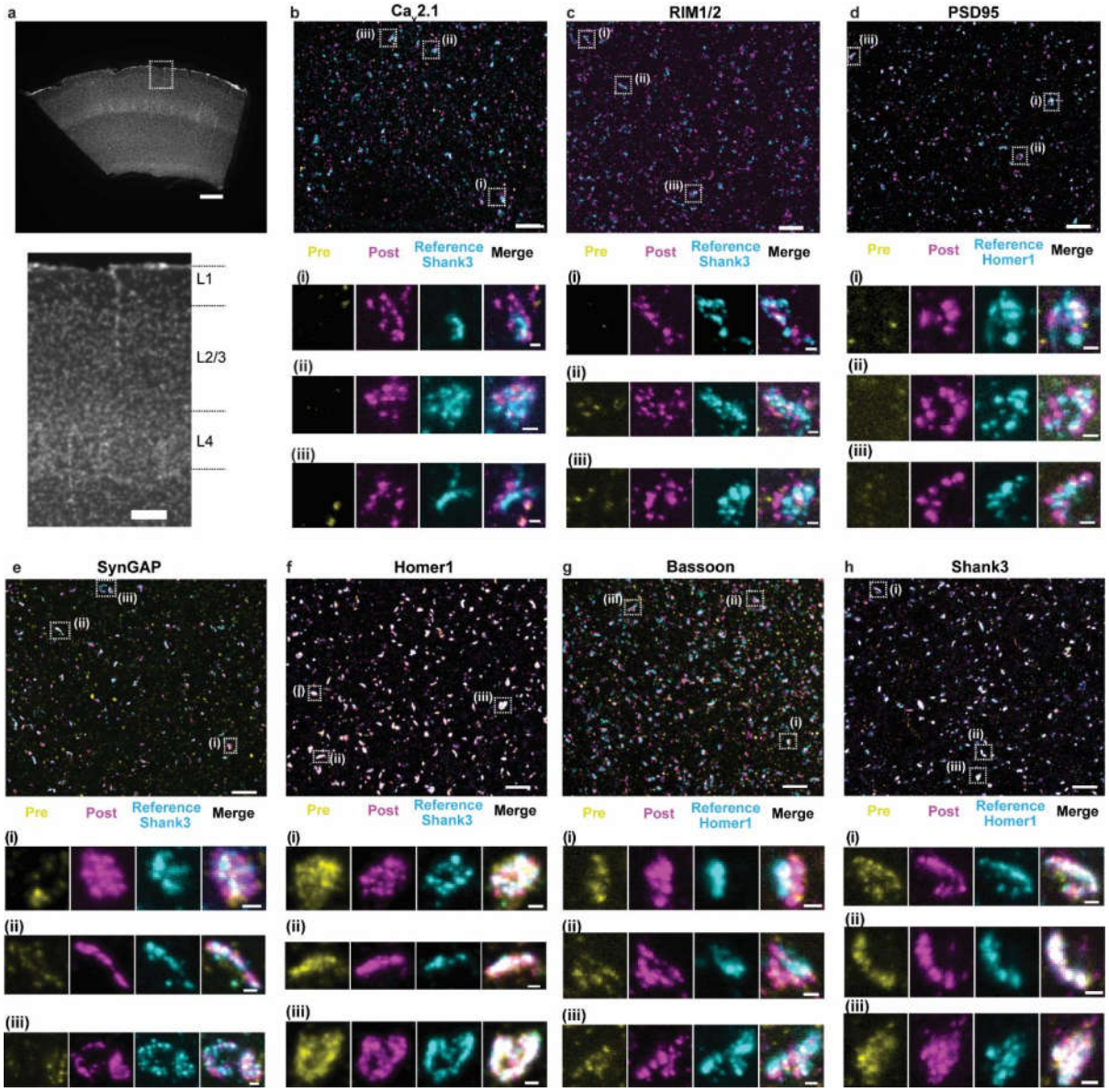
a
L1
L2/3
L4
b
Ca$_V$2.1
c
RIM1/2
d
PSD95
Pre
Post
Reference Shank3
Merge
Reference Homer1
(i)
(ii)
(iii)
e
SynGAP
f
Homer1
g
Bassoon
h
Shank3

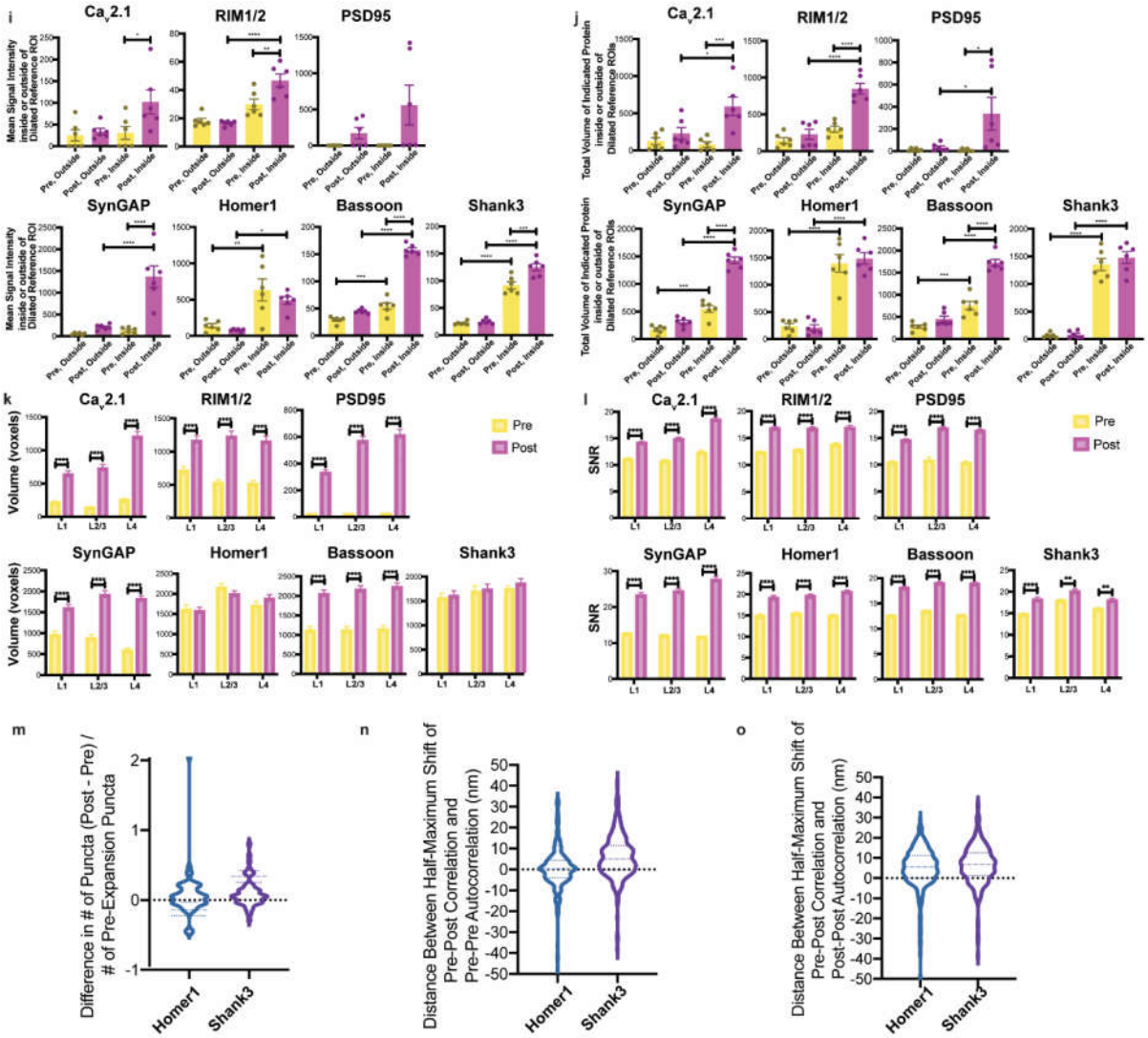

Figure 2 | Validation of ExR enhancement and effective resolution in synapses of mouse cortex. (a) Low-magnification widefield image of a mouse brain slice with DAPI staining showing somatosensory cortex (top) and zoomed-in image (bottom) of boxed region containing L1, L2/3, and L4, which are imaged and analyzed after expansion further in panels **b-h**. (Scale bar, 300 µm (top) and 100 µm (bottom)). **(b-h)** Confocal images of (max intensity projections) of specimen after immunostaining with antibodies against $Ca_v2.1$ (Ca^{2+} channel P/Q-type) **(b)**, RIM1/2 **(c)**, PSD95 **(d)**, SynGAP **(e)**, Homer1 **(f)**, Bassoon **(g)**, and Shank3 **(h),** in somatosensory cortex L2/3. For pre-expansion staining, primary and secondary antibodies were stained before expansion, the stained secondary antibodies anchored to the gel, and finally fluorescent tertiary antibodies applied after expansion to enable visualization of pre-expansion staining. For post-expansion staining, the same primary and secondary antibodies were applied after ExR. Antibodies against Shank3 **(b, c, e, f)** or Homer1 **(d, g, h)** were applied post-expansion as a reference channel. Confocal images of cortex L2/3 (top) show merged images of pre- and post-expansion staining, and the reference channel. Zoomed-in images of three regions

boxed in the top image (**i-iii,** bottom) show separate channels of pre-expansion staining (yellow), post-expansion staining (magenta), reference staining (cyan), and merged channel. (Scale bar, 1.5 µm (upper panel); 150 nm (bottom panel of i-iii).) **(i,j)** Quantification of decrowding in a set of manually identified synapses. Statistical significance was determined using Sidak's multiple comparisons test following ANOVA (*P≤0.05, **P≤0.01, ***P < 0.001, ****P < 0.0001, here and throughout the paper, and plotted is the mean, with error bars representing standard error of the mean (SEM), here and throughout the paper). (**i)** Mean signal intensity inside and outside of (i.e., nearby to) dilated reference ROIs for pre- and post-expansion stained manually-identified synapses (see **Supplementary Table 1** for numbers of technical and biological replicates)). Data points represent the mean across all synapses from a single field of view. (**j)** Total volume (in voxels; 1 voxel = 17.16x17.15x40, or 11,779, nm^3) of signals inside and outside of dilated reference ROIs, in both cases within cropped images containing one visually identified synapse (see **Supplementary Fig. 3h**), for pre- and post-expansion stained manually-identified synapses (see **Supplementary Table 1** for numbers of biological and technical replicates). Data points represent the mean across all synapses from a single field of view. **(k)** Mean voxel size and **(l)** mean signal-to-noise (SNR) ratio of pre- and post-expansion immunostaining showing 7 proteins in somatosensory cortex regions L1, L2/3, and L4 of 2 mice. Plotted is mean and SEM. To compare the 3D voxel size and SNR of pre- and post-expansion stained synapses for each of the seven proteins, three t-tests (one for each layer) were run (n = 49-70 puncta per layer from 2 mice; see **Supplementary Table 1** for replicate numbers). Statistical significance was determined using multiple t-tests corrected using the Holm-Sidak method, with alpha = 0.05. **(m)** Population distribution (violin plot of density, with a dashed line at the median and dotted lines at the quartiles) of the difference in the number of synaptic puncta between post- and pre-expansion staining channels for Homer1 and Shank3 (Homer1, n = 304 synapses from 2 mice; Shank3, n = 309 synapses from 2 mice. **(n)** Population distribution of the difference in distance (in nm) between the half-maximal shift for pre-pre autocorrelation and post-pre correlation (calculated pixel-wise between intensity values normalized to the minimum and maximum of the image, see Methods) averaged over x-, y-, and z-directions (x- and y-directions being transverse, z-direction being axial) for Homer1 and Shank3 (Homer1, n = 303 synapses from 2 mice, Shank3, n = 305 synapses from 2 mice). **(o)** Population distribution of the difference in distance (in nm) between the half-maximal shift for post-post autocorrelation and post-pre correlation (calculated pixel-wise between intensity values normalized to the minimum and maximum of the image) averaged over x-, y-, and z-directions for Homer1 and Shank3 (Homer1, n = 303 synapses from 2 mice, Shank3, n = 305 synapses from 2 mice).

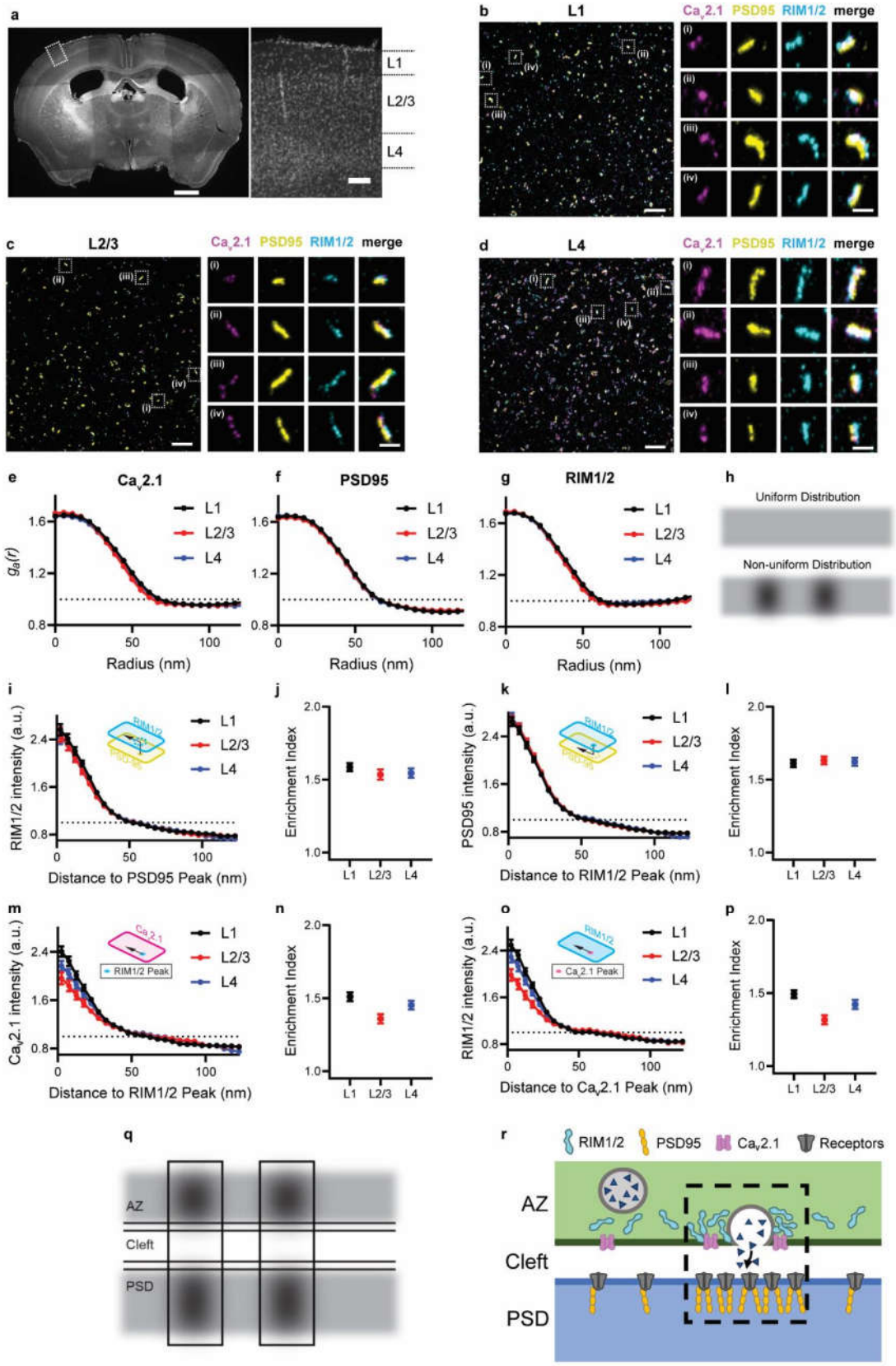
a
L1
L2/3
L4
b
L1
Ca$_v$2.1 PSD95 RIM1/2 merge
c
L2/3
Ca$_v$2.1 PSD95 RIM1/2 merge
d
L4
Ca$_v$2.1 PSD95 RIM1/2 merge
e
Ca$_v$2.1
f
PSD95
g
RIM1/2
$g_a(r)$
Radius (nm)
h
Uniform Distribution
Non-uniform Distribution
i
RIM1/2 intensity (a.u.)
Distance to PSD95 Peak (nm)
j
Enrichment Index
k
PSD95 intensity (a.u.)
Distance to RIM1/2 Peak (nm)
l
m
Ca$_v$2.1 intensity (a.u.)
Distance to RIM1/2 Peak (nm)
n
o
RIM1/2 intensity (a.u.)
Distance to Ca$_v$2.1 Peak (nm)
p
q
AZ
Cleft
PSD
r
RIM1/2
PSD95
Ca$_v$2.1
Receptors
AZ
Cleft
PSD

Figure 3 | ExR reveals how calcium channel distributions participate in transsynaptic nanoarchitecture. (a) Low-magnification widefield image of DAPI stained mouse brain slice (left) and zoomed in view (right) of the boxed region showing layers 1-4 of the cortex. (Scale bar = 1000 µm (left panel of whole brain) and 100 µm (right panel of the layers 1-4). **(b-d)** show confocal images (max intensity projections) of layers 1, 2/3 and 4 respectively, after performing ExR and immunostaining with antibodies against $Ca_V2.1$ (calcium channel) (magenta), PSD95 (yellow) and RIM1/2 (cyan). In each of (b), (c) and (d), low magnification images are shown on the left while zoomed-in images of four regions, i-iv are shown on the right with separated channels for each antibody along with the merged image. (Scale bar = 1 µm (left panel) and 100 nm (right panels labeled i-iv)). **(e-g)** show the autocorrelation analysis for $Ca_V2.1$, PSD95 and RIM1/2 respectively for different layers, from which it is evident that these proteins have non-uniform distribution forming nanoclusters instead of having a uniform distribution as illustrated in **(h)**. **(i), (k), (m)** and **(o)** show the enrichment analysis that calculates the average molecular density for RIM1/2 to the PSD95 peak, PSD95 to the RIM1/2 peak, $Ca_V2.1$ to the RIM1/2 peak and RIM1/2 to the $Ca_V2.1$ peak respectively while **(j), (l), (n)** and **(p)** show the corresponding mean enrichment indexes respectively. Error bars indicate SEM. **(q)** Schematic illustration represents that the nanoclusters of any two proteins (RIM1/2, PSD95 and $Ca_V2.1$) are aligned with nanoscale precision with each other. This may lead to efficient use of calcium ions in vesicle fusion as calcium channels are located close to vesicle fusion sites (dictated by RIM1/2) as well as efficient transfer of neurotransmitters across the synapse as the vesicle fusion site is located directly opposite to the location of receptor sites (PSD95 being a scaffolding protein) as schematically illustrated in **(r)**.

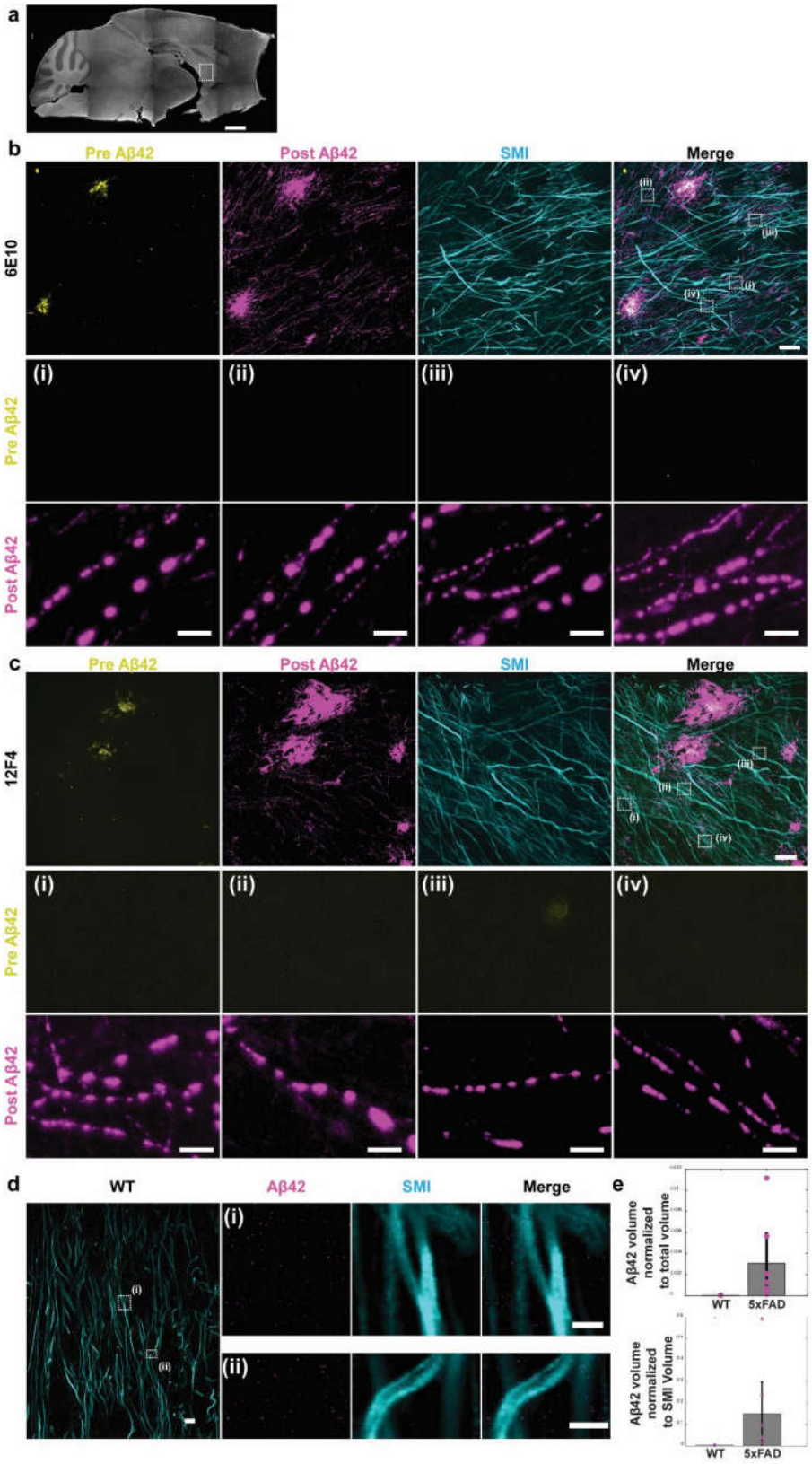
a
b
Pre Aβ42
Post Aβ42
SMI
Merge
6E10
(i)
(ii)
(iii)
(iv)
Pre Aβ42
Post Aβ42
c
Pre Aβ42
Post Aβ42
SMI
Merge
12F4
(i)
(ii)
(iii)
(iv)
Pre Aβ42
Post Aβ42
d
WT
Aβ42
SMI
Merge
(i)
(ii)
e
Aβ42 volume normalized to total volume
WT
5xFAD
Aβ42 volume normalized to SMI Volume
WT
5xFAD

Figure 4 | ExR reveals periodic nanoclusters of Aβ42 peptide in the fornix of Alzheimer's model 5xFAD mice. (a) Epifluorescence image showing a sagittal section of a 5xFAD mouse brain with the fornix highlighted. (Scale bar, 1000 μm) **(b-c)** ExR confocal Images (max intensity projections) showing immunolabeling against Aβ42 peptide with two different monoclonal antibodies 6E10 (b) and 12F4 (c). From left to right: pre-expansion immunolabeling of Aβ42 (yellow), post-expansion labeling (magenta) of Aβ42, post-expansion SMI (neurofilament protein), and merged pre- and post-expansion staining of Aβ42 with post-expansion staining of SMI. Insets (i-iv) show regions of interest highlighted in the merged images in the fourth column; top panels, pre-expansion labeling; bottom panels, post-expansion labeling. Post-ExR staining reveals periodic nanostructures of β-amyloid, whereas pre-expansion staining can detect only large plaque centers. (Scale bar = 10 μm (upper panel images); 1 μm (bottom panels, i-iv)) **(d)** ExR confocal images showing post-expansion Aβ42 (magenta) and SMI (cyan) staining in wild-type (WT) mice. Left image, low magnification image in the fornix. Insets (i) and (ii), close-up views of Aβ42 and SMI staining patterns from boxed regions in the left image. (Scale bar = 4 μm (left panel); 1 μm (right panels, i-ii)) **(e)** Histograms showing the volume of Aβ42 clusters and aggregates in WT and 5xFAD specimens normalized to the total field of view (FOV) volume (top) or the volume of SMI (bottom). Two sample Kolmogorov-Smirnov test, p-values < 0.001. N= 14 data points (7 per condition) from 14 FOVs from 4 mice (2 mice per condition).

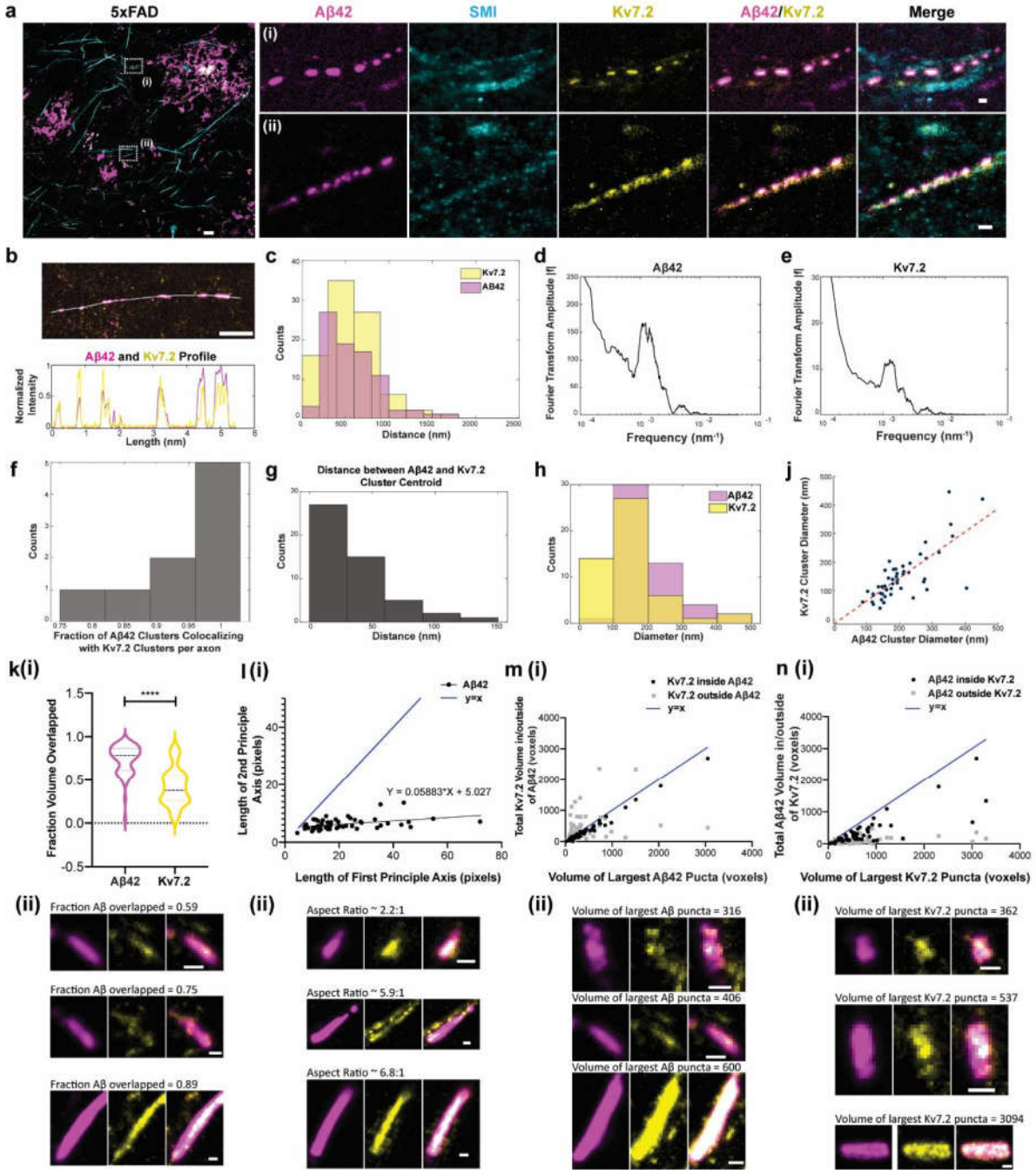

Figure 5 | ExR reveals co-localized clusters of Aβ42 peptide and potassium ion channels in the fornix of Alzheimer's model 5xFAD mice. (a) ExR confocal image (max intensity projections) showing post-expansion Aβ42 (magenta), SMI (cyan) and Kv7.2 (yellow) staining in the fornix of a 5xFAD mouse. Leftmost panel, merged low magnification image. (Scale bar = 4 μm); insets (i-ii) show close-up views of the boxed regions in the leftmost image for Aβ42, SMI, Kv7.2, Aβ42-Kv7.2 merged and Aβ42-Kv7.2-SMI merged respectively (scale bar = 400

nm; n = 5 fields of view from 2 slices from 2 mice) **(b)** ExR confocal image (max intensity projections) showing Aβ42 (magenta) and Kv7.2 (yellow) clusters in a 5xFAD mouse (top) with the indicated cross-section profile shown (bottom). (Scale bar = 1 μm) **(c)** Histograms showing distances between adjacent Aβ42 (magenta) and K_v7.2 (yellow) clusters in 5xFAD mice along imaged segments of axons (n=97 Aβ42 clusters, 92 Kv7.2 clusters from 9 axonal segments from 2 mice). **(d-e)** Fourier transformed plots of Aβ42 (d) and K_v7.2 (e) showing the same peak position (from the same data set as (**c**)). **(f)** Histogram showing the fraction of Aβ42 clusters colocalizing with K_v7.2 clusters along individual segments of axons (n=50 cluster pairs from 9 axonal segments from 2 mice). **(g)** Histogram showing the distance between the centroids of colocalized Aβ42 and K_v7.2 clusters (same data set as (f)). **(h)** Histograms showing the diameters of Aβ42 clusters (magenta) and K_v7.2 clusters (yellow) (n=50 cluster pairs from 9 axonal segments from 2 mice). **(j)** Scatter plot showing the diameters of colocalized Aβ42 and K_v7.2 clusters. **(k)(i)** Fraction of total Aβ42 and K_v7.2 puncta volume overlapped with one another in cropped Aβ42 clusters (n = 55 clusters from 2 5xFAD mice; $p < 0.0001$, pairwise t-test). ****P < 0.0001. **(k)(ii)** Representative images illustrating the difference in the proportion of mutually overlapped volume between Aβ42 and Kv7.2 as a fraction of total Aβ42 or Kv7.2 volume (scale bar = 100nm). **(l)(i)** Length of the second principal axis of the ellipsoid that has the same normalized second central moments as the largest Aβ42 punctum in an ROI, vs. the length of the first principal axis of this ellipsoid (in pixels, 1 pixel = 11.44 nm in x- and y-directions (transverse) and 26.67nm in the z-direction (axial); black points represent individual manually cropped ROIs; slope of best-fit line from simple linear regression = 0.05883, $p = 0.0020$, $F = 10.59$, df = 53). Compare to the line y = x (blue). **(l)(ii)** Representative images illustrating the oblong shape of Aβ42 puncta, for three first principal axis lengths: shorter (top row), medium (middle row) and longer (bottom row). While the length of the first principal axis varies significantly between these examples, the length of the second principal axis remains similar between the three clusters. **(m)(i)** Total volume (in voxels, 1 voxel = 11.44x11.44x26.67 or 3,490 nm^3) of K_v7.2 puncta overlapped/inside (black, $R^2 = 0.980$, $p < 0.0001$) and outside (gray, $R^2 = 0.0582$, $p = 0.0979$) Aβ42 puncta, as a function of the volume of the largest Aβ42 puncta within an ROI, compared to the line y = x (blue). **(m)(ii)** Representative images illustrating that the volume of K_v7.2 outside of Aβ42 is relatively constant as Aβ42 puncta size increases. As in **(l)(ii)**, the three clusters shown are ordered by increasing size. **(n)** The converse of **(m)**: total volume of Aβ42 puncta overlapped/inside (black, $R^2 = 0.6531$, $p < 0.0001$) and outside (gray, $R^2 = 0.1876$, $p = 0.0010$) of K_v7.2 puncta, as a function of the volume of the largest K_v7.2 puncta within an ROI, compared to the line y = x (blue). **(n)(ii)**. Representative images illustrating that the volume of Aβ42 outside of K_v7.2 is smaller than the volume of Aβ42 co-localized with K_v7.2, and both values are positively correlated with the volume of the largest K_v7.2 puncta. Scale bar of (**k-n ii**) = 100 nm.

Methods

Brain tissue preparation

All procedures involving animals were in accordance with the US National Institutes of Health Guide for the Care and Use of Laboratory Animals and approved by the Massachusetts Institute of Technology Committee on Animal Care. Both male and female wild type mice (C57BL/6 or Thy1-YFP) and 5xFAD mice were used, because of the current study's focus on developing and validating a novel technology. Mice were deeply anesthetized using isoflurane in room air. Mice were transcardially perfused at room temperature with ice cold 10 mL of 2 % (w/v) acrylamide in phosphate buffered saline (PBS) followed by ice cold 10 mL of 30 % acrylamide (w/v) and 4% paraformaldehyde in PBS. Brains were harvested and incubated in 20 mL of the same fixative solution (30 % acrylamide and 4% paraformaldehyde in PBS) at 4°C overnight. Fixed brains were transferred to 100 mM glycine at 4 °C for 6 h, then stored in PBS at 4°C for long term storage or sectioned to 50-100 µm-thick slices with a vibrating microtome (Leica VT1000S).

Expansion of brain tissue slices

For the 1st gelling step, brain slices were incubated in the 1st gelling solution (8.625% (w/v) sodium acrylate (SA), 2.5% (w/v) acrylamide (AA), 0.075% (w/v) N,N'-methylenebisacrylamide (Bis), 0.2% (w/v) ammonium persulfate (APS) initiator, 0.2% (w/v) tetramethylethylenediamine (TEMED) accelerator, 0.2% (w/v), 0.01% 4-Hydroxy-TEMPO (HT)) for 30 min at 4°C. Slices were embedded in 4 well dish gelling chambers on cover glasses surrounded by excess 1st gelling solution, and incubated at 37°C for 2 h. After the incubation, gels containing the tissue were cut out from the chamber and incubated with denaturation buffer (200 mM SDS, 200 mM NaCl, and 50 mM Tris pH 9)[1] for 1 h at 95°C. Denatured gels were fully expanded via 4 washes for 15 min each with 5 mL distilled (DI) water in a 6 well-plate.

For the re-embedding step, expanded 1st gels were incubated in re-embedding solution (13.75% (w/v) AA, 0.038% (w/v) Bis, 0.025% (w/v) APS, 0.025% (w/v) TEMED) twice, replacing the first solution with freshly made re-embedding solution for 1 h each time on a shaker at room temperature. The re-embedded gels were transferred to a 4 well dish gelling chamber on cover glasses and incubated with excess re-embedding solution for 2 h at 45°C. The re-embedded gels were washed 3 times for 15 min each with 5 mL PBS in a 6 well-plate.

For the 3rd gelling step, the re-embedded gels were incubated in 3rd gelling solution (8.625% (w/v) SA, 2.5% (w/v) AA, 0.038% (w/v) Bis, 0.025% (APS), 0.025% (w/v) TEMED) twice,

replacing the first solution with fresh made 3rd gelling solution for 1 h each time on a shaker at room temperature. The 3rd gels were placed in a 4 well dish gelling chamber on cover glasses and incubated at 60 °C for 1 h.

Gels were fully expanded in DI water by changing excess water 5 times for 2 h each and trimming axially to reduce thickness to 1 mm to facilitate subsequent immunostaining and imaging.

Immunostaining of expanded tissues

Expanded gels were incubated in blocking solution (0.5% Triton X-100, 5% normal donkey serum (NDS) in PBS) for 2 h at room temperature. Gels were then incubated with primary antibodies (see Methods Antibody list) in '0.25T' blocking buffer (0.25% Triton X-100, 5% NDS in PBS) overnight at 4°C. Gels were washed in washing buffer (0.1% Triton X-100 in PBS) 6 times for 1 h each time on a shaker at room temperature. Gels were then incubated with secondary antibodies in blocking solution overnight at 4°C, and washed in washing buffer 6 times for 1 h each on a shaker at room temperature.

Decrowding experiments

Fig 2b-h: Nanoscale-resolution imaging of synapses in somatosensory cortex. For pre-expansion antibody staining, brain slices were incubated with primary antibodies in blocking solution overnight at 4°C. Stained tissues were washed in washing buffer 6 times for 1 hr each time on a shaker at room temperature. Secondary antibodies (100 µL, 1 mg/mL) were incubated with 6-((acryloyl)amino)hexanoic acid, succinimidyl ester (AcX) (2 µL, 1 mg/mL) overnight at room temperature to prepare AcX conjugated secondary antibodies. Primary antibody stained tissues were then incubated with AcX-secondary antibodies in blocking solution overnight at 4°C, and washed in washing buffer 6 times for 1 h each time on a shaker at room temperature. Tissue expansion was carried out the same as previously described. The tertiary antibodies were stained after expansion to bind against AcX-secondary antibodies to visualize the pre-expansion staining.

For post-expansion antibody staining, expanded gels were incubated with the same primary and secondary antibodies without AcX conjugation. Antibodies against Shank3 or Homer1 were provided as a reference channel after expansion.

Quantification and validation of the decrowding effect

Fig. 2i-j. Decrowding analysis of manually segmented synapses. We compared the amplitude of signal intensity in the foreground (putative synapses) and background (everything else). First, we manually identified, based on brightness and size of reference channel staining, 47-70 of the largest, brightest synapses per ~350x350x20 micron (physical units) field of view (see **Supplementary Table 1** for exact numbers of synapses; one field of view per cortical layer, three cortical layers per sample, two mice per synaptic protein). We developed an automated method to segment putative synaptic puncta from background. First, background was subtracted from image stacks using ImageJ/Fiji's Rolling Ball algorithm with a radius of 50 pixels. Images were then binarized using a threshold calculated as seven times the standard deviation of the average intensity of manually-identified background regions selected every 10th slice of the z-stack. Binary images were passed through a 3-D median filter of radius 5x5x3 pixels to remove small puncta of non-specific staining. We then identified 3-D connected components from the filtered binary stack using MATLAB's "bwconncomp" function, with a pixel connectivity of 26, meaning that pixels are connected if their faces, edges, or corners touch. Connected components smaller than $120x120x120nm^3$ (biological units) were removed, as most synapses are larger than this volume. ROIs, or putative synaptic puncta, were defined as 3-D connected components of the filtered, binary reference stack dilated using a disk structuring element with a radius of six pixels. A radius of six pixels (~100nm, in biological units) was chosen because both pre- and post-synaptic proteins of the same synapse, but not other synapses, fall within this range (the synaptic cleft is ~12-20nm^2), which we confirmed by manual inspection. Segmented synapses with zero filtered connected components (synaptic puncta) in the reference channel were excluded from further analysis. We calculated the average intensity of background-subtracted images either within or outside of these dilated reference ROIs (**Fig. 2i**) to measure signal increase within putative synapses relative to signal increase in the background. All images were acquired under the same microscope conditions to allow for comparison of mean signal intensity. The total volume of pre- or post-expansion staining test puncta located within dilated reference channel ROIs (**Fig. 2j**) was calculated from binarized stacks of pre- and post-expansion channels (thresholded and filtered as described for the reference channel) after multiplying the dilated binary reference stack (for inside dilated reference ROIs) or its inverse (for just outside dilated reference ROIs, but still within the manually-cropped synaptic area) by the binary pre- or post-expansion stack and calculating the sum of nonzero voxels for each product. Data are shown as the mean of each measure across the ~50 synapses per field of view, and the deviation was calculated as the standard error of these means across the six fields of view for each protein.

Fig. 2k-l. Quantification of synaptic properties. To compare volume and signal-to-noise ratio (SNR) of pre- and post-expansion staining, we used the same dataset for Fig. 2i, j analysis. First, the background was subtracted from image stacks using ImageJ/Fiji's Rolling Ball algorithm with a radius of 50 pixels. Images were then binarized using a threshold calculated as seven times the standard deviation of the average intensity of manually-identified background regions

selected every 10th slice of the z-stack. We then identified and selected the biggest 3-D connected components in pre- and post-staining test channels separately in each layer of somatosensory cortex (L1, L2/3 and L4, respectively), as these are the most likely to be synapses. We calculated the voxel and signal intensity in the largest 3-D connected components from 49-70 manually selected synapses (see **Supplementary Table 1** for exact numbers for each layer, protein, and mouse). The signal intensity was divided by the standard deviation of the background intensity to calculate SNR.

Fig. 2m-n and Supplementary Fig. 5: Analysis of distortion introduced by ExR relative to pre-expansion staining.

To calculate the number of synaptic puncta, background-subtracted images were first thresholded as described previously (based on a multiple of the standard deviation of manually-identified background regions) and passed through a 3x3x5 voxel (1 voxel = 17.16x17.16x40nm^3) median filter. MATLAB's "bwconncomp" function was used to find connected components (putative synaptic puncta, connectivity of 26), and connected components with fewer than 30 voxels of volume were excluded from further analysis. For the plots shown in **Supplementary Fig. 5g-l**, images were shifted by one voxel in each direction and padded using the intensity values of the pixels that were shifted out at that step. To calculate pixel-wise correlations and autocorrelations (**Supplementary Fig. 5g-h**), images were first normalized to their minimum and maximum intensity values. From these, we calculated the pairwise linear correlation coefficient (MATLAB's "corr") between pixel intensity values in the pre- and post-expansion staining channels, or pre-(/post-) and pre(/post)-expansion staining channels for autocorrelation. To calculate the half-maximal shift distance (**Fig. 2n-o**), we fit a third-degree polynomial (MATLAB's "fit" with "poly3") to the correlation or autocorrelation as a function of shift distance, and used the best-fit curve to estimate the shift distance at which the correlation or autocorrelation reached 50% of its maximum value. For the plots shown in **Supplementary Fig. 5i-j,** the correlation was calculated with a slight modification to account for differences in puncta volume. First, background-subtracted images were masked based on the corresponding binary image. Second, nonzero pixels were divided by the mean intensity value in the nonzero regions. Finally, the correlation was calculated as the pairwise linear correlation coefficient (MATLAB's "corr") between masked, mean-normalized intensity values in the pre- and post-expansion staining channels. Mutually overlapped volume was calculated as the sum of nonzero pixels in intersection of the binary pre- and post-expansion staining z-stacks, and normalized to the total puncta volume (sum of nonzero pixels in the binary z-stack) in the pre-expansion staining channel (**Supplementary Fig. 5k-l**). Each of these calculations was repeated for each shift in the x-, y-, and z-directions. Synapses with zero puncta in the pre- or post-expansion staining channels were excluded from analysis.

Comparison between antigen retrieval and decrowding effect

Supplementary Fig. 2. Confocal images after immunostaining with antibodies against $Ca_v2.1$, PSD95 and Homer1 with or without antigen retrieval treatment to compare signal quality for antigen retrieval vs. ExR treatment. To determine whether antigen retrieval by heat denaturation alone is the dominant factor underlying increased signal quality afforded by ExR, we treated one group of tissues with a standard antigen-retrieval step (placing tissues in 20 mM sodium citrate at pH 8 and incubating at 100°C for 30 sec and 60°C for 30 min)[3]. Tissues with or without this antigen-retrieval step were processed by ExR. Then, we compared the amplitude of signal intensity in foreground (putative synapses) and background (everything else). First, we manually identified, based on brightness and size of reference channel staining (Homer1 for Cav2.1, Shank3 for PSD95 and Homer1), 30 of the largest and brightest synapses per ~350x350x20 micron (physical units) field of view (n = 30 synapses from 1 field of view from 1 mouse). We used the automated segmentation procedure and calculated mean signal intensity and volume as described above (see "Decrowding analysis of manually segmented synapses").

Protein distance measurement and Synaptic nanocolumn results analysis

Fig 1h, Fig 3e-g, Fig 3i-p. For analysis, potential synapses were manually identified and selected based on 1) the juxtaposition of presynaptic clusters and postsynaptic clusters, and 2) the colocalization of clusters on the same side of the synapse. As camera pixel size was 167 nm (physical units) and the step size of the z-stack was 250 nm (physical units), the voxel size was not equivalent in all dimensions. Because isometric voxels were necessary for subsequent analysis, each voxel was then subdivided into 12 smaller isometric voxels, each 83.3 nm (physical units) in all three dimensions. For comparisons of RIM1/2 and PSD95, one cluster was shifted in space to optimally overlap with the other cluster, as previously described[4,5]. The vector of this shift was determined by cross-correlation of the two clusters, and defined both the transsynaptic axis and the distance between the two clusters. For comparisons of RIM1/2 and $Ca_v2.1$, the shift distance was set as 0, and for comparisons of RIM1/2 and PSD95, putative synapses with a RIM1/2 to PSD95 peak-to-peak distance of less than 20 or greater than 180 nm (biological units) were rejected from further analysis, consistent with the dimensions of the active zone and PSD. Any synapses that extended beyond the z-range of the imaged stack were also excluded.

The autocorrelation ($g_a(r)$) and the protein enrichment analyses were adapted from previously described localization data-based analyses (Tang et al., 2016; Chen et al, 2020). The 3D autocorrelation function ($g_a(r)$) tests the general homogeneity of density within a defined volume. Because the function was normalized by the correlation of a homogenized object with the same shape and volume, homogeneous fluorescence within a synaptic cluster will give a $g_a(r) = 1$ at all radii, and local intensity peaks will result in a $g_a(r) > 1$ over a radius of the size of region of high intensity. The cluster boundary was defined based on fluorescent intensity after convolution with a spherical kernel (r ~ 300 nm).

The relative molecular distribution within two different protein clusters was characterized using a cross-enrichment analysis. The enrichment analysis was performed by measuring the angularly averaged voxel intensity as a function of the distance from the point of peak intensity in the reference channel, and then normalizing this value by the angularly averaged intensity (as a function of the distance from the point of peak intensity in the reference channel) based on an object of the same shape and volume as the real object with voxels set to the average intensity of the real object. The enrichment index was calculated by taking the average of the enrichment values within a radius of 60 nm from the peak of the reference channel.

Synapse numbers (n) for the analysis from 2 mice:

Autocorrelations

Cav2.1 (Fig. 3e): n = 144 synapses (Layer 1), 101 synapses (Layer 23), 103 synapses (Layer 4)

PSD95 (Fig. 3f): n = 144 synapses (Layer 1), 101 synapses (Layer 23), 103 synapses (Layer 4)

RIM1/2 (Fig. 3g): n = 144 synapses (Layer 1), 101 synapses (Layer 23), 103 synapses (Layer 4)

Enrichment analysis

RIM1/2 enrichment to PSD95 peak (Fig. 3i-j): n = 153 synapses (Layer 1), 103 synapses (Layer 23), 108 synapses (Layer 4)

PSD95 enrichment to RIM1/2 peak (Fig. 3k-l): n = 152 synapses (Layer 1), 102 synapses (Layer 23), 108 synapses (Layer 4)

$Ca_v2.1$ enrichment to RIM1/2 peak (Fig. 3m-n): n = 150 synapses (Layer 1), 103 synapses (Layer 23), 107 synapses (Layer 4)

RIM1/2 enrichment to $Ca_v2.1$ peak (Fig. 3o-p): n = 153 synapses (Layer 1), 99 synapses (Layer 23), 108 synapses (Layer 4)

Enrichment Index values (mean +/- S.D.):

RIM1/2 to PSD-95 peak (Fig. 3j): 1.585 +/- 0.330 (Layer 1), 1.535 +/- 0.358 (Layer 23), 1.545 +/- 0.332 (Layer 4)

PSD-95 to RIM1/2 peak (Fig. 3l): 1.611 +/- 0.308 (Layer 1), 1.632 +/- 0.269 (Layer 23), 1.622 +/- 0.285 (Layer 4)

$Ca_v2.1$ to RIM1/2 peak (Fig. 3n): 1.510 +/- 0.364 (Layer 1), 1.359 +/- 0.330 (Layer 23), 1.452 +/- 0.314 (Layer 4)

RIM1/2 to $Ca_V2.1$ peak (Fig. 3p): 1.493 +/- 0.330 (Layer 1), 1.317 +/- 0.311 (Layer 23), 1.422 +/- 0.322 (Layer 4)

Alzheimer's results analysis

Fig. 4e. Comparison of Aβ42 volume in WT vs 5xFAD. 3D image stacks of Aβ42 and SMI312 staining were background subtracted via rolling-ball background subtraction with a 200px radius using ImageJ/Fiji. For each color channel, the standard deviation for the background was calculated using a 75x75px window. Subsequently, each color channel was binarized by applying a threshold of 28 times the STD of the background. This value was determined by evaluating the amount of thresholding required to remove putative non-specific staining spots. Finally, after binarization, the volume of Aβ42 and SMI312 for each field of view (FOV) was determined by adding up the segmented pixels of each color channel.

Fig. 5c. Distance Measurement between Clusters. To calculate the distance between adjacent clusters for either Aβ42 or $K_V7.2$, clusters that line along SMI312 neurofilaments were manually cropped out in 3D. Then, after applying rolling-ball background subtraction with a 100px radius, the centroid of each cluster was annotated manually using ImageJ/Fiji in 3D. Given that the spacing between clusters is much larger than the size of each cluster, we reasoned that manual labeling of the centroids incurs minimal error. Finally, the distance between adjacent clusters was calculated in 3D.

Fig. 5g-j. Calculation of Aβ42 and $K_V7.2$ Cluster Diameter. After applying rolling-ball background subtraction with a 100px radius to 3D FOVs of Aβ42 and $K_V7.2$ staining, overlapping $K_V7.2$ and Aβ42 clusters were manually cropped out. After calculating the standard deviation of the background of each channel, the cropped images were binarized by applying a threshold ten times the standard deviation of the background. The volume of each cluster was then identified via Connected-Component analysis using MATLAB's "bwconncomp" function. Finally, the centroid and principal axis length of each cluster were determined using the associated "regionprops" function, which models each connected component region as an ellipsoid. The centroid values were then used to calculate the distance between overlapped Aβ42 and $K_V7.2$ clusters.

Fig. 5k-n. Aβ42 and Kv7.2 Cluster Shape Analysis. ROIs containing single Aβ42 puncta that were part of a periodic chain-like structure were manually identified (n = 55 ROIs, 5 ROIs per field of view, from 11 fields of view from two mice) from background-subtracted images (ImageJ/Fiji's Rolling Ball algorithm, radius of 50 pixels). To visualize the 3D shape of Aβ42

and K_v7.2 puncta within these ROIs, we resliced the image stack along both transverse dimensions, at equal spacing to the axial dimension. We display the middle slice in each stack in the x-y plane in **Fig. 5k(ii)-n(ii)** and the middle slice in each stack in the x-y, y-z, and x-z planes in **Supplementary Fig. 11a** (where x- and y-directions are transverse, and z-direction is axial). To quantify shape features, we used CellProfiler's[6] Watershed[7] segmentation module to segment puncta within manually extracted ROIs, using a footprint of 30 pixels for each channel. A custom MATLAB script was deployed to calculate the number of puncta in each channel, mean and maximum volume and surface area of these puncta, length of the three principal axes of the ellipsoid that have the same normalized second central moments as the region for the largest puncta, and the total volume of puncta overlap between Aβ42 and K_v7.2 as the number of non-zero pixels in the intersection of the binary image stacks. To quantify the statistical significance of the relationships between these measures, either two-tailed paired t-tests or simple linear regression were used as described in the text.

Expansion factor and root mean square error measurement

Supplementary Fig. 1. A Thy1-YFP mouse was perfused as described above and 50 µm coronal sections were prepared using a vibratome. Before expansion, YFP fluorescence was imaged in six fields of view from the cortex of three cortical slices. Subsequently, these slices were processed with the ExR protocol as described above. Expanded slices were then labeled with a primary antibody against GFP (thermo Fisher A-11122) and a secondary antibody (see Methods Antibody list). The same fields of view imaged pre-expansion were identified and confocal images were acquired of the antibody staining. Pre and post ExR images were acquired on an Andor spinning disk (CSU-X1 Yokogawa) confocal microscope with a 40 × 1.15 numerical aperture water objective.

To determine distortion arising from the process of ExR, pre and post expansion images were aligned and deformations in images were determined as described previously[8]. Briefly, pre and post ExR images were background subtracted with a Rolling Ball background subtraction algorithim (ImageJ/Fiji) with a 200 px radius. Then, corresponding confocal planes from pre and post images were identified and registered using Fiji's Turboreg method allowing for scaling and rigid rotation. Then, a custom MATLAB script was used to implement a B-spline based non-rigid registration between pre and post expansion images, yielding vector fields for deformation within the images. These vector fields were then used to calculate root-mean-square length distortions across varying lengths.

List of chemicals

Product Name	Vendor	Product Number
Sodium acrylate	Santa Cruz	CAS7446-81-3
Acrylamide	Sigma	A9099
N,N′-Methylenebisacrylamide (BIS)	Sigma	M7279
Ammonium persulfate (APS)	Sigma	A3678
N,N,N′,N′-Tetramethylethylenediamine (TEMED)	Sigma	T7024
4-Hydroxy-TEMPO (HT)	Sigma	176141
6-((acryloyl)amino)hexanoic Acid, Succinimidyl Ester (AcX)	Thermo Fisher	A20770
Sodium dodecyl sulfate (SDS)	Sigma	436143
Sodium Chloride (NaCl)	Thermo Fisher	AM9760
Tris Buffer	Fisher scientific	77-86-1
Paraformaldehyde	Electron Microscopy Sciences	15710
Triton X-100	Sigma	X100
Glycine	Sigma	50046
PBS 10x	Thermo Fisher	70011044
Normal Donkey Serum	Jackson ImmunoResearch	017-000-121

Sodium citrate dihydrate	Sigma	W302600

List of antibodies

Primary / Secondary	Target	Host	Vendor	Product number	Dilution
Primary	Cav1.2	Guinea pig	Synaptic Systems	152 205	1:200
Primary	RIM1/2	Rabbit	Synaptic Systems	140 203	1:200
Primary	PSD95	Mouse	Thermo Fisher	MA1-046	1:200
Primary	PSD95	Rabbit	Cell Signaling Technology	CST3450S	1:200
Primary	SynGAP	Rabbit	Thermo Fisher	PA1-046	1:200
Primary	Homer1	Rabbit	Synaptic Systems	160 003	1:200
Primary	Bassoon	Rabbit	Synaptic Systems	141 003	1:200
Primary	Shank3	Guinea pig	Synaptic Systems	162 304	1:200
Primary	Aβ42 (6E10)	Mouse	BioLegend	SIG39320	1:200
Primary	Aβ42 (12F4)	Mouse	BioLegend	SIG39142	1:200
Primary	Aβ42 (D54D2)	Rabbit	Cell Signaling Technology	CST8243S	1:200
Primary	SMI	Chicken	Abcam	ab4680	1:400
Primary	Kv7.2	Mouse	Santa Cruz	sc-271852	1:200

Primary	Nav1.6	Rabbit	Abcam	ab65166	1:200
Secondary	Mouse	Goat	ThermoFisher	A28175 (Alexa Fluor 488 nm)	1:200
Secondary	Mouse	Goat	ThermoFisher	A11031 (Alexa Fluor 546 nm)	1:200
Secondary	Mouse	Donkey	Biotium	20124 (CF 633 nm)	1:200
Secondary	Mouse	Donkey	ThermoFisher	A10036 (Alexa Fluor 546 nm)	1:200
Secondary	Rabbit	Goat	ThermoFisher	A11034 (Alexa Fluor 488 nm)	1:200
Secondary	Rabbit	Goat	ThermoFisher	A11035 (Alexa Fluor 546 nm)	1:200
Secondary	Rabbit	Donkey	Biotium	20125 (CF 633 nm)	1:200
Secondary	Rabbit	Donkey	ThermoFisher	A10040 (Alexa Fluor 546 nm)	1:200
Secondary	Guinea pig	Donkey	Biotium	20171 (CF 633 nm)	1:200
Secondary	Chicken	Goat	ThermoFisher	A11039 (Alexa Fluor 488 nm)	1:200
Secondary	Chicken	Donkey	Biotium	20168 (CF 633 nm)	1:200

Gel solution of ExR

Chemical	1st gel solution	Re-embedding solution	3rd gel solution
Sodium acrylate	8.625 %	-	8.625 %

Acrylamide	2.5 %	13.75 %	2.5 %
Bis	0.075 %	0.038 %	0.038 %
HT	0.01 %	-	-
TEMED	0.2 %	0.025 %	0.025 %
APS	0.2 %	0.025 %	0.025 %

All composition is w/v%.

ExR Procedure

1. Mouse tissue slices

i. Anesthetize mice using isoflurane in oxygen and perfuse with 10 mL of 2% acrylamide in PBS followed by 10 mL of 30% acrylamide and 4% paraformaldehyde in PBS.

ii. Harvest brains and incubate in 20 mL of the same fixative solution (30% acrylamide and 4% formaldehyde in PBS) at 4°C overnight.

iii. Transfer fixed brains to 100 mM Glycine at 4°C for 6 h.

iv. Store tissues in PBS at 4°C for long term storage.

v. Slice tissues on a vibrating microtome to a thickness of 50-100 µm.

2. Gellation

A. Gelling for 1st expansion

i. Incubate brain slices in the 1st gelling solution for 30 min at 4°C.

ii. Place brain slices with excess 1st gelling solution between two #1.5 coverglass separated by two pieces of #1.5 coverglass, and then incubate at 37°C for 2 h.

iii. Cut out gels from the chamber and incubate with denaturation buffer (200 mM SDS, 200 mM NaCl, and 50 mM Tris pH 9) for 1 h at 95°C.

iv. Wash gels 4 times with DI water in shaker and expand gels in DI water at 4°C overnight.

B. Re-embedding

i. Incubate expanded 1st gels in re-embedding solution twice for 1 h each time in shaker at room temperature.

ii. Transfer gels between #1.5 coverglass separated by slide glass and incubate with excess re-embedding solution at 45°C for 2 h.

iii. Wash gels 3 times with PBS in shaker.

C. 3rd gelling

i. Incubate the re-embedded gels in the 3rd gelling solution twice for 1 h each time in shaker at room temperature.

ii. Transfer gels between #1.5 coverglass separated by slide glass and incubate at 60°C for 1 h.

iii. Wash gels 4 times with DI water in shaker and expand gels in DI water at 4°C overnight.

iv. Trim gels axially to 1 mm thickness.

3. Staining

i. Incubate gels in blocking solution (0.5% Triton X-100, 5% normal donkey serum (NDS) in PBS) for 2 h at room temperature.

ii. Incubate gels with primary antibodies in '0.25T' blocking buffer (0.25% Triton X-100, 5% NDS in PBS) overnight at 4°C.

iii. Wash gels with washing buffer (0.1% Triton X-100 in PBS) 6 times for 1 h each time.

iv. Incubate gels with secondary antibodies in blocking solution at 4°C overnight.

v. Wash gels with washing buffer (0.1% Triton X-100 in PBS) 6 times for 1 h each time and expand gels in DI water for 20x expansion or 0.05x PBS for 15x expansion.

Methods References

1. Ku, T. *et al.* Multiplexed and scalable super-resolution imaging of three-dimensional protein localization in size-adjustable tissues. *Nat. Biotechnol.* **34**, 973–981 (2016).

2. Savtchenko, L. P. & Rusakov, D. A. The optimal height of the synaptic cleft. *Proc. Natl. Acad. Sci. U. S. A.* **104**, 1823–1828 (2007).

3. Zhao, Y. *et al.* Nanoscale imaging of clinical specimens using pathology-optimized expansion microscopy. *Nat. Biotechnol.* (2017) doi:10.1038/nbt.3892.

4. Tang, A. H. *et al.* A trans-synaptic nanocolumn aligns neurotransmitter release to receptors. *Nature* (2016) doi:10.1038/nature19058.

5. Chen, J. H., Blanpied, T. A. & Tang, A. H. Quantification of trans-synaptic protein alignment: A data analysis case for single-molecule localization microscopy. *Methods*

6. McQuin, C. *et al.* CellProfiler 3.0: Next-generation image processing for biology. *PLOS Biol.* **16**, e2005970 (2018).

7. Mangan, A. P. & Whitaker, R. T. Partitioning 3D surface meshes using watershed segmentation. *IEEE Trans. Vis. Comput. Graph.* **5**, 308–321 (1999).

8. Chen, F., Tillberg, P. W. & Boyden, E. S. Expansion microscopy. *Science* **347**, 543–548 (2015).

Acknowledgments

We thank T. Biederer, C. Zhang and Y. Liu for antibody advice, S. Alon and K. Piatkevich for trainings and discussions and B. Kang for decrowding analysis advice. D. S. acknowledges funding from NIH K99/R00 Pathway to independence Award, M.E.S was supported by the National Science Foundation Graduate Research Fellowship under Grant No. 1745302, A.H.T.

acknowledges funding from NARSAD. L.H.T. acknowledges funding from Ludwig Family Foundation, the JPB Foundation, NIH Grants RO1 NS102730 and RF1 AG054321, T.A.B acknowledges funding from NIMH R37MH080046, E.S.B. acknowledges funding from the Ludwig Family Foundation, the Open Philanthropy Project, John Doerr, Lisa Yang and the Tan-Yang Center for Autism Research at MIT, U. S. Army Research Laboratory and the U. S. Army Research Office under contract/grant number W911NF1510548, NIH Director's Pioneer Award 1DP1NS087724, NIH R01MH110932, NIH R01EB024261, NIH U24NS109113, NIH R37MH08004613, NIH 1RM1HG008525, and the HHMI-Simons Faculty Scholars Program. Thanks to Brian Chow and Eric Betzig, as well as to many current and past members of the Synthetic Neurobiology group, for discussions.

The funders had no role in study design, data collection and analysis, decision to publish, or preparation of the manuscript.

Author Contributions

D.S. initiated work, developed ExR technology, contributed key ideas, designed and performed experiments and interpreted data for all projects, and wrote and edited the manuscript. J.K. contributed key ideas, designed and performed experiments for all projects, performed analysis for decrowding, and wrote and edited the manuscript. A.T.W. co-developed approaches to measuring decrowding, contributed key ideas to ExR technology development and decrowding analysis, designed and performed experiments, analyzed data for all projects, and wrote and edited the manuscript. M.E.S contributed key ideas, designed and implemented analysis, visualization, and statistical tests for all projects, created Fig. 1 schematic with input from others, and wrote and edited the manuscript. Z.P. contributed key ideas, designed and performed experiments and did analysis for the Alzheimers project. T.B.T. contributed key ideas, designed experiments, created software, analyzed and interpreted data related to synapses, and helped in writing and editing the manuscript. A.T. created software and analyzed data related to synapses. E.N. designed experiments, interpreted experimental data for the Alzheimers project as well as helped in writing and editing the manuscript. J. Z. Y. oversaw the Alzheimer's project and designed experiments for it. L. H. T conceptualized and initiated the Alzheimer's project, provided oversight and funding, contributed key ideas and designed experiments as well as helped in writing and editing the manuscript. T.A.B. contributed key ideas, designed experiments and interpreted data for the synapse project as well as helped in writing and editing the manuscript. E.S.B. supervised the project, initiated work, contributed key ideas, designed experiments, helped with data analysis and interpretation, and wrote and edited the manuscript.

Competing Interest Declaration

D.S., A.T.W., J.K., and E.S.B. are co-inventors on a patent application for ExR. E.S.B. is co-founder of a company seeking to deploy medical applications of ExM-related technologies.